A multilayer shallow model for dry granular flows with the $\mu(I)$-rheology: application to granular collapse on erodible beds

E.D. Fernández-Nieto [*], J. Garres-Díaz [†], A. Mangeney [‡§], G. Narbona-Reina [*]

Abstract

In this work we present a multilayer shallow model to approximate the Navier-Stokes equations with the $\mu(I)$-rheology through an asymptotic analysis. The main advantages of this approximation are (i) the low cost associated with the numerical treatment of the free surface of the modelled flows, (ii) theexact conservation of mass and (iii) the ability to compute 2D profiles of the velocities in the directions along and normal to the slope. The derivation of the model follows Fernández-Nieto *et al. (J. Comput. Phys.*, vol. 60, 2014, pp. 408-437) and introduces a dimensional analysis based on the shallow flow hypothesis. The proposed first-order multilayer model fully satisfies a dissipative energy equation. A comparison with steady uniform Bagnold flow – with and without the sidewall friction effect – and laboratory experiments with a non-constant normal profile of the downslope velocity demonstrates the accuracy of the numerical model. Finally, by comparing the numerical results with experimental data on granular collapses, we show that the proposed multilayer model with the $\mu(I)$-rheology qualitatively reproduces the effect of the erodible bed on granular flow dynamics and deposits, such as the increase of runout distance with increasing thickness of the erodible bed. We show that the use of a constant friction coefficient in the multilayer model leads to the opposite behaviour. This multilayer model captures the strong change in shape of the velocity profile (from S-shaped to Bagnold-like) observed during the different phases of the highly transient flow, including the presence of static and flowing zones within the granular column.

[*]Dpto. Matemática Aplicada I. ETS Arquitectura - Universidad de Sevilla. Avda. Reina Mercedes S/N, 41012-Sevilla, Spain, (edofer@us.es, gnarbona@us.es)

[†]IMUS & Dpto. Matemática Aplicada I. ETS Arquitectura - Universidad de Sevilla. Avda. Reina Mercedes S/N, 41012-Sevilla, Spain, (jgarres@us.es)

[‡]IInstitut de Physique du Globe de Paris, Seismology team, University Paris-Diderot, Sorbonne Paris Cité, 75238, Paris, France, (mangeney@ipgp.fr)

[§]ANGE team, CEREMA, INRIA, Lab. J. Louis Lions, 75252, Paris, France

Contents

1 Introduction **2**

2 The initial system **5**
2.1 Governing equations 5
2.2 $\mu(I)$-rheology 5
2.3 Boundary conditions 7
2.4 Local coordinates 7

3 The $\mu(I)$-rheology multilayer model **8**
3.1 Dimensional analysis 8
3.2 A multilayer approach 10
3.2.1 Notation 10
3.2.2 Weak solution with discontinuities 11
3.3 Final model 14

4 Numerical tests **16**
4.1 Granular surface flows in channel 16
4.1.1 Steady uniform Bagnold flow: analytical solution 17
4.1.2 2D steady uniform flow in a channel: sidewalls effect on the velocity profile 19
4.1.3 Laboratory experiments: transient velocity profiles 20
4.2 Granular collapse experiments 21
4.2.1 Improvement of the approximation of the $\mu(I)$ coefficient 22
4.2.2 Experimental and test data 23
4.2.3 Deposit profiles 24
4.2.4 Effect of the erodible bed 26
4.2.5 Flow dynamics and velocity profiles 28

5 Conclusions **33**

A Derivation of the multilayer model **34**
A.1 Mass conservation 35
A.2 Momentum conservation 35

1 Introduction

Granular flows have been widely studied in recent years because of their importance in industrial processes and geophysical flows such as avalanches, debris or rock avalanches, landslides, etc. In particular, numerical modelling of geophysical granular flows provides a unique tool for hazard assessment.

The behaviour of real geophysical flows is very complex due to topography effects, the heterogeneity of the material involved, the presence of fluid phases, fragmentation, etc. ([18]). One of the major issues is to quantify erosion/deposition processes that play a key role in geophysical flow dynamics but are very difficult to measure in the field (see e. g. [17, 29, 9]). Laboratory experiments on granular flows are very useful to test flow models on simple configurations where detailed measurements can be performed, even if some physical processes may differ between the large and small scale. These experiments may help in defining appropriate rheological laws to describe the behaviour of granular materials. Recent experiments by Mangenet *et al.* [38] and Farin *et al.* [21] on granular column collapse have quantified how the dynamics and deposits of dry granular flows change in the presence of an erodible bed. They showed a significant increase

of the runout distance (i.e. maximum distance reached by the deposit) and flow duration with increasing thickness of the erodible bed. This strong effect of bed entrainment was observed only for flows on slopes higher than a critical angle of approximately 16° for glass beads. The question remains as to whether this behaviour can be reproduced by granular flow models.

Understanding the rheological behaviour of granular material is a major challenge. In particular, a key issue is to describe the transition between flow (fluid-like) and no-flow (solid-like) behaviour. Granular flows have been described by viscoplastic laws and especially by the so-called $\mu(I)$-rheology, introduced by Jop *et al.* [32]. It specifies that the friction coefficient μ is variable and depends on the inertial number I that is related to the pressure and strain rate. Jop *et al.* [33] considered this viscoplastic law and compared their results with laboratory experiments to investigate the time evolution of the vertical profile of velocity in narrow channels, where the sidewall friction is modelled through an additional friction term introduced by [31]. Lagrée *et al.* [34] implemented the $\mu(I)$-rheology in a full Navier-Stokes solver (Gerris) by defining a viscosity from the $\mu(I)$-rheology. They validated the model with 2D analytical solutions and compared it to 2D discrete element simulations of granular collapses over horizontal rigid beds and with other rheologies. Staron *et al.* [50, 51] applied this model to granular flows in a silo. Using an augmented Lagrangian method combined with finite element discretisation to solve the 2D full Navier-Stokes equations, Ionescu *et al.* [28] showed that this rheology quantitatively reproduces laboratory experiments of granular collapses over horizontal and inclined planes. By interpreting the $\mu(I)$-rheology as a viscoplastic flow with a Drucker-Prager yield stress criterion and a viscosity depending on the pressure and strain rate, they showed that the mean value of this viscosity has a key impact on the simulated front dynamics and on the deposit of granular column collapses. In particular without viscosity, the runout distance is strongly overestimated. However using a constant viscosity or a spatio-temporally variable viscosity only slightly changes the results for granular column of small aspect ratio (see [28]).

In [16], the authors implemented the $\mu(I)$-rheology in a three-dimensional numerical model with a finite element method combined with the Newton-Raphson algorithm with a regularization technique. The numerical model was validated by an analytical solution for a dry granular vertical-chute flow and a dry granular flow over an inclined plane and by laboratory experiments. Previously, Chauchat & Médale [15] simulated the bed-load transport problem in 2D and 3D with a two-phase model that considers a Drucker-Prager rheology for the granular phase. Lusso *et al.* [36] used a finite element method to simulate a 2D viscoplastic flow considering a Drucker-Prager yield stress criterion and a constant viscosity. They obtained similar results taking into account either a regularization method or the augmented Lagrangian algorithm. By comparing the simulated normal velocity profiles and the time change of the position of the flow/no-flow (i. e. flowing/static) interface with laboratory experiments by Farin *et al.* [21], they concluded that a pressure and rate-dependent viscosity can be important to study flows over an erodible bed. A similar conclusion is presented in [35] after comparing the normal velocity profiles and the position of the flow/no-flow interface during the stopping phase of granular flows over erodible beds calculated with a simplified thin-layer but not depth-averaged viscoplastic model ([13]) with those measured in laboratory experiments.

Because of the high computational cost of solving the full 3D Navier-Stokes equations, in particular in a geophysical context, granular flows have often been simulated using depth-averaged shallow models. The shallow or thin-layer approximation (the thickness of the flow is assumed to be small compared to its downslope extension) associated with depth-averaging leads to conservation laws like the Saint-Venant equations. These approximations have been applied to granular flows by Savage & Hutter [47] by assuming a Coulomb friction law where the shear stress at the bottom is proportional to the normal stress, with a constant friction coefficient μ. However, this model does not reproduce the increase in runout distance observed with increasing thickness of the erodible bed. The analytical solution deduced in [20] proves that this model leads to the opposite effect. The question is as to whether this opposite behaviour between the experiments and simulations

is due to the thin-layer approximation and/or depth-averaging process or to the rheological law implemented in the model (i.e. constant friction coefficient).

Recently, Capart *et al.* [14] proposed a depth-integrated model taking into account a linearization of the $\mu(I)$-rheology. They prescribed an S-shaped velocity profile corresponding to equilibrium debris flows and typical of granular flows over erodible beds. Their velocity profiles were reconstructed using the computed averaged velocity making it possible to compare their results with velocity profiles measured in laboratory experiments. Gray & Edwards [26] introduced the $\mu(I)$-rheology in a depth-averaged model by adding a viscous term and prescribing a Bagnold velocity profile, typical of granular flows over rigid beds. Edwards & Gray [19] showed the ability of this model to capture roll-waves and erosion-deposition waves, if it is combined with the basal friction law introduced in [45]. In these two depth-averaged models, however, the shape of the velocity profile is prescribed so that they cannot reproduce the different profiles observed in highly transient flows such as in granular collapses where the velocity profiles change from Bagnold-like near the front to S-shaped upstream where upper grains flow above static grains (see [28]). Furthermore, in depth-averaged models, only the mean velocity over the whole thickness of the flow is calculated (i.e., the whole granular column is either flowing or at rest, except for the model proposed by Capart *et al.* [14]). Granular collapse experiments and simulations have shown on the contrary that during the stopping phase and when erosion/deposition processes occur, static zones may develop near the bottom and propagate upwards. The resulting normal gradient of the downslope velocity, which changes in time, is a significant term in the strain rate and therefore strongly influences the $\mu(I)$ coefficient. The well-posedness of the full $\mu(I)$-rheology is proved by Barker *et al.* [7] for a large intermediate range of values of the inertial number I. It is ill-posed for low and high values of I, even for steady-uniform flows where I ranges from zero to infinity when the slope varies between the limit angles of the $\mu(I)$-rheology.

Multilayer models represent an interesting alternative to depth-averaged models, making it possible in particular to resolve the shape of velocity profiles. They were introduced by Audusse [1] and extended by Audusse *et al.* [4]. A different multilayer model, which takes into account the exchange of mass and momentum between the layers, has since been derived by Audusse *et al.* [3, 5], and Sainte-Marie [46].

A new procedure to obtain a multilayer model has been introduced by Fernández-Nieto *et al.* [23]. Several differences appear between this multilayer model and the ones deduced by Audusse *et al.* First, in [23], the multilayer model is derived from the variational formulation of Navier-Stokes equations with hydrostatic pressure by considering a discontinuous profile of the solution at the interfaces of a vertical partition of the domain. This procedure proves that the solution of this multilayer model is a particular weak solution of the Navier-Stokes system. Moreover, the mass and momentum transfer terms at the interfaces of the normal partition are deduced from the jump conditions verified by the weak solutions of the Navier-Stokes system. In addition, the definition of the vertical velocity profile is easily obtained using the mass jump condition combined with the incompressibility condition.

By comparing this model with granular flow experiments on erodible beds ([33, 38, 21]), we evaluate (i) if the model with the $\mu(I)$-rheology gives a reasonable approximation of the granular flow dynamics in different regimes and of their deposits, (ii) if the model is able to reproduce strong changes in velocity profiles during highly transient flows, (iii) if it reproduces the increase in runout distance observed for granular collapses for increasing thickness of the erodible bed above a critical slope angle $\theta_c \in [12^o, 16^o]$ and (iv) how the multilayer approach improves the results compared to the classical depth-averaged Saint-Venant model (i.e. monolayer model).

The paper is organised as follows. Section 2 is devoted to presenting the initial system composed of the 2D Navier-Stokes equations with the $\mu(I)$-rheology and the appropriate boundary conditions. We also give the local coordinates system that we consider for the derivation. In Section 3 we present the multilayer approach following [23] to derive a 2D multilayer model for dry granular flows up to first order when considering the thin-layer asymptotic approximation.

The final $\mu(I)$-rheology Multilayer Shallow Model (MSM) is also presented in this section together with the associated energy balance. Section 4 is devoted to presenting the numerical results. First, we validate our model using the 2D analytical solution of a Bagnold flow and a flow in a narrow channel with a strong effect of the lateral wall friction. We also compare with experimental data for the previous case, and do a deeper comparison of our results with granular collapse laboratory experiments done by Mangeney *et al.* [38]. We show that the $\mu(I)$-rheology is able to qualitatively reproduce the increase in runout distance of granular flows over erodible beds, in contrast with the constant friction model. Moreover, the multilayer approach reproduces the change in shape of the velocity profiles and significantly improves results compared to the monolayer one (i.e. Saint-Venant). Finally, conclusions are presented in Section 5.

2 The initial system

In this section we present the two-dimensional model considered to describe the dynamics of granular flows. First, we introduce the starting system of equations, completed with the definition of the stress tensor including the $\mu(I)$-rheology. We then specify the suitable boundary conditions. Finally, we present the complete model in local coordinates.

2.1 Governing equations

We consider a granular mass flow with velocity $\boldsymbol{u} \in \mathbb{R}^2$ and density $\rho \in \mathbb{R}$ and we set the incompressible Navier-Stokes equations describing the dynamics of the system:

$$\begin{cases} \nabla \cdot \boldsymbol{u} \ = \ 0, \\ \\ \rho \partial_t \boldsymbol{u} \ + \ \rho \nabla \cdot (\boldsymbol{u} \otimes \boldsymbol{u}) - \nabla \cdot \boldsymbol{\sigma} \ = \rho \, \boldsymbol{g}, \end{cases} \tag{1}$$

where $\boldsymbol{g}$ is the gravity force. The total stress tensor is

$$\boldsymbol{\sigma} = -p\boldsymbol{\mathcal{I}} + \boldsymbol{\tau}, \tag{2}$$

with $p \in \mathbb{R}$ the pressure. $\boldsymbol{\mathcal{I}}$ is the 2D identity tensor and $\boldsymbol{\tau}$ the deviatoric stress tensor given by

$$\boldsymbol{\tau} = \eta D(\boldsymbol{u}),$$

where $\eta \in \mathbb{R}$ denotes the viscosity and $D(\boldsymbol{u})$ the strain-rate tensor

$$D(\boldsymbol{u}) = \frac{1}{2}(\nabla \boldsymbol{u} + (\nabla \boldsymbol{u})').$$

2.2 $\mu(I)$-rheology

As discussed in the Introduction, we consider the so-called $\mu(I)$-rheology (see [32]) in order to take into account the non-Newtonian nature of granular flows. Hence, the viscosity coefficient is defined by

$$\eta = \frac{\mu(I)p}{\|D(\boldsymbol{u})\|}, \tag{3}$$

with $\|D\| = \sqrt{0.5 \; D : D}$ the usual second invariant of a tensor D. The friction coefficient $\mu(I)$ is written as

$$\mu(I) = \mu_s + \frac{\mu_2 - \mu_s}{I_0 + I} I,$$

where I_0 is a constant value and $\mu_2 > \mu_s$ are constant parameters. I is the inertial number

$$I = \frac{2d_s\|D(\boldsymbol{u})\|}{\sqrt{p/\rho_s}}, \tag{4}$$

where d_s is the particle diameter and ρ_s the particle density. The apparent flow density is then defined as

$$\rho = \varphi_s \rho_s, \tag{5}$$

where the solid volume fraction, denoted by φ_s, is assumed to be constant.

Note that when the shear rate is equal to zero, $\mu(I)$ is reduced to μ_s. For high values of the inertial number, $\mu(I)$ converges to μ_2. Otherwise, if we consider a constant value of μ, independent of I, the model is always ill-posed (see [48]).

The $\mu(I)$-rheology includes a Drucker-Prager plasticity criterion, the deviatoric tensor is defined as

$$\begin{cases} \boldsymbol{\tau} = \dfrac{\mu(I)p}{\|D\|}\, D & \text{if } \|D\| \neq 0, \\ \\ \|\boldsymbol{\tau}\| \leq \mu_s p & \text{if } \|D\| = 0. \end{cases}$$

Note that the $\mu(I)$-rheology can equivalently be written as a decomposition of the deviatoric stress in a sum of a plastic term and a rate-dependent viscous term (see [28]):

$$\begin{cases} \boldsymbol{\tau} = \dfrac{\mu_s p}{\|D\|} D + 2\tilde{\eta} D & \text{if } \|D\| \neq 0, \\ \\ \|\boldsymbol{\tau}\| \leq \mu_s p & \text{if } \|D\| = 0; \end{cases}$$

with a viscosity defined as $\tilde{\eta} = \dfrac{(\mu_2 - \mu_s)p}{\frac{I_0}{d_s}\sqrt{p/\rho_s} + 2\|D\|}$. Here we investigate the rheology defined by a variable friction $\mu(I)$ and a constant friction μ_s. In [28], the authors showed that simulations of the front propagation of granular column collapses and of their deposits are very sensitive to the value of the average value of the viscosity (see their figures 8 and 13). However, replacing $\tilde{\eta}$ by a constant viscosity equal to the averaged value of the spatio-temporal viscosity $\tilde{\eta}$ does not significantly change the simulated dynamics and deposit. Here we compare the case where $\mu = \mu_s$ so that $\tilde{\eta} = 0$ with the $\mu(I)$ rheology corresponding to typical values of the viscosity $\eta = 1$ Pa·s for granular collapses over horizontal and inclined planes ([28]).

The model considering a viscosity defined by (3) presents a discontinuity when $\|D(\boldsymbol{u})\| = 0$. To avoid this singularity there are several ways to proceed. One of them is to apply a duality method, such as augmented Lagrangian methods ([25]) or the Bermúdez-Moreno algorithm ([10]). Another option is to use a regularization of $D(\boldsymbol{u})$, which is cheaper computationally; however it does not give an exact solution, contrary to duality methods.

In this work, we take into consideration two kinds of regularizations of $D(\boldsymbol{u})$. First, we use the regularization proposed in [34], which consist of bounding the viscosity by $\eta_M = 250\rho\sqrt{gh^3}$ Pa·s, considering instead of (3),

$$\eta = \frac{\mu(I)p}{\max\left(\|D(\boldsymbol{u})\|, \frac{\mu(I)p}{\eta_M}\right)}. \tag{6}$$

In this way, we obtain $\eta = \eta_M$ if $\|D(\boldsymbol{u})\|$ is close to zero. We used this regularization in the simulation of the granular flow experiments. However, as explained in Section 4.1, we cannot consider this regularization in some tests presented below, for which we have to take into account the regularization introduced in [8],

$$\eta = \frac{\mu(I)p}{\sqrt{\|D(\boldsymbol{u})\|^2 + \delta^2}},$$

where $\delta > 0$ is a small parameter.

2.3 Boundary conditions

We consider the usual geometric setting, that is, the granular material fills a spatial domain limited by a fixed topography at the bottom and by a free surface at the top.

Since the domain is moved with the velocity of the material, we set the kinematic condition

$$N_t + \boldsymbol{u} \cdot \boldsymbol{n}^h = 0, \text{ at the free surface,} \tag{7}$$

with $(N_t, \boldsymbol{n}^h)$ the time-space normal vector to the free surface. We also assume a normal stress balance

$$p = 0, \text{ at the free surface.} \tag{8}$$

At the bottom we consider the no-penetration condition

$$\boldsymbol{u} \cdot \boldsymbol{n}^b = 0, \text{ at the bottom,} \tag{9}$$

where $\boldsymbol{n}^b$ is the downward unit normal vector to the bottom. We also consider a Coulomb-type friction law involving the variable friction coefficient $\mu(I)$:

$$\boldsymbol{\sigma}\, \boldsymbol{n}^b - \left(\left(\boldsymbol{\sigma}\, \boldsymbol{n}^b\right) \cdot \boldsymbol{n}^b\right) \boldsymbol{n}^b = \begin{pmatrix} \mu(I)p\dfrac{u}{|u|} \\ \\ 0 \end{pmatrix}, \text{ at the bottom.} \tag{10}$$

Note that the multilayer approach considered here can also be deduced by considering a no-slip condition, that is, $\boldsymbol{u} = \boldsymbol{0}$ at the bottom. This condition implies the no penetration condition (9). Then, the only difference is that instead of considering condition (10), the definition of $\boldsymbol{\sigma}\, \boldsymbol{n}^b - \left(\left(\boldsymbol{\sigma}\, \boldsymbol{n}^b\right) \cdot \boldsymbol{n}^b\right) \boldsymbol{n}^b$ at the bottom must be set by using the no-slip condition and the profile of $\boldsymbol{u}$ (see [26]). The resulting model with this alternative condition is analysed at the end of Subsection 3.3.

2.4 Local coordinates

Let us consider tilted coordinates, which are commonly used for granular flows (see [22, 42, 26, 12, 13]). Let $\widetilde{b}(x)$ be an inclined fixed plane of constant angle θ with respect to the horizontal axis; we define the coordinates $(x, z) \in \Omega \times \mathbb{R}^+ \subset \mathbb{R}^2$. The x and z axis are measured along the inclined plane and along the normal direction respectively (see figure 1). In this reference frame the gravitational force is written as

$$\boldsymbol{g} = (-g\ \sin\ \theta, -g\ \cos\ \theta)'.$$

In addition, we set $b(x)$ an arbitrary bottom topography and a layer of the material over it with thickness $h(t,x)$. Both are measured in the normal direction to the inclined plane $\widetilde{b}(x)$. We consider the velocity $\boldsymbol{u} \in \mathbb{R}^2$ with horizontal (downslope direction) and vertical (normal direction) components (u,w). We set $\nabla = (\partial_x, \partial_z)$, the usual differential operator in the space variables.

With these definitions we write:

$$\boldsymbol{\tau} = \begin{pmatrix} \tau_{xx} & \tau_{xz} \\ \tau_{xz} & \tau_{zz} \end{pmatrix} \quad \text{and} \quad D(\boldsymbol{u}) = \frac{1}{2}\begin{pmatrix} 2\partial_x u & \partial_z u + \partial_x w \\ \partial_z u + \partial_x w & 2\partial_z w \end{pmatrix}.$$

In this reference frame, system (1) can be developed as

$$\begin{cases} \partial_x u + \partial_z w = 0, \\ \rho\big(\partial_t u + u\,\partial_x u + w\,\partial_z u\big) + \partial_x p = -\rho g \sin\theta + \partial_x \tau_{xx} + \partial_z \tau_{xz}, \\ \rho\big(\partial_t w + u\,\partial_x w + w\,\partial_z w\big) + \partial_z p = -\rho g \cos\ \theta + \partial_x \tau_{xz} + \partial_z \tau_{zz}. \end{cases} \tag{11}$$

For the boundary conditions (7)-(10) we just take into account the definitions of the normal vectors. Namely, the time and space normal vectors to the free surface are respectively

$$N_t = \partial_t h; \qquad \boldsymbol{n}^h = \frac{(\partial_x(b+h), -1)}{\sqrt{1 + |\partial_x(b+h)|^2}};$$

and the normal vector to the bottom reads:

$$\boldsymbol{n}^b = \frac{(\partial_x b, -1)}{\sqrt{1 + |\partial_x b|^2}}.$$

3 The $\mu(I)$-rheology multilayer model

In this section, we present a multilayer model designed to approximate the dynamics of granular flows. We follow [23], in which a multilayer approach was developed to solve the Navier-Stokes equations. In our case, the system to approximate is given by the equations (11) together with the boundary conditions described in Section 2.3. The originality of this paper is to develop the multilayer approach together with an asymptotic approximation. The system is deduced under several specific changes involving the asymptotic approximation and the definition of the stress tensor according to the $\mu(I)$-rheology that introduces a non-constant viscosity coefficient. The advantage of this approach is that we recover the normal profile of the downslope and normal components of the velocity.

In the first subsection we show the dimensional analysis of the equations and write the non-dimensional system in matrix form. In the second part we present a brief explanation of the procedure to obtain the multilayer model and the model itself. A more detailed presentation of the deduction is made in Appendix A, where we focus on the aspects of the derivation that differ from the method proposed in [23].

3.1 Dimensional analysis

In this subsection we carry out a dimensional analysis of the system (1)-(10) under the local coordinates system specified in Section 2.4. We consider a shallow domain by assuming that the

ratio $\varepsilon = H/L$ between the characteristic height H and the characteristic length L is small. We also introduce the characteristic density ρ_0. Following the scaling analysis proposed in [26], we define the dimensionless variables, denoted with the tilde symbol $(\widetilde{.})$, as follows:

$$(x, z, t) = (L\widetilde{x}, H\widetilde{z}, (L/U)\widetilde{t}), \quad (u, w) = (U\widetilde{u}, \varepsilon U\widetilde{w}),$$

$$h = H\widetilde{h}, \quad \rho = \rho_0\widetilde{\rho}, \quad p = \rho_0 U^2\widetilde{p},$$

$$\eta = \rho_0 U H\widetilde{\eta}, \quad \eta_M = \rho_0 U H\widetilde{\eta_M},$$

$$(\tau_{xx}, \tau_{xz}, \tau_{zz}) = \rho_0 U^2 \left(\varepsilon\widetilde{\tau_{xx}}, \widetilde{\tau_{xz}}, \varepsilon\widetilde{\tau_{zz}}\right).$$

Let us also note that

$$D(\boldsymbol{u}) = \frac{U}{H}\ \frac{1}{2}\begin{pmatrix} 2\varepsilon\partial_{\widetilde{x}}\widetilde{u} & \partial_{\widetilde{z}}\widetilde{u} + \varepsilon^2\partial_{\widetilde{x}}\widetilde{w} \\ \partial_{\widetilde{z}}\widetilde{u} + \varepsilon^2\partial_{\widetilde{x}}\widetilde{w} & 2\varepsilon\partial_{\widetilde{z}}\widetilde{w} \end{pmatrix},$$

and the Froude number

$$Fr = \frac{U}{\sqrt{g\cos\theta H}}.$$

Then, the system of equations (11) can be rewritten using this change of variables as (tildes have been dropped for simplicity):

$$\begin{cases} \partial_x u + \partial_z w \ = \ 0, \\ \rho\big(\partial_t u + u\partial_x u + w\partial_z u\big) + \partial_x p = -\dfrac{1}{\varepsilon}\rho\dfrac{1}{Fr^2}\tan\ \theta + \varepsilon\partial_x\tau_{xx} + \dfrac{1}{\varepsilon}\partial_z\tau_{xz}, \\ \varepsilon^2\rho\big(\partial_t w + u\partial_x w + w\partial_z w\big) + \partial_z p = -\rho\dfrac{1}{Fr^2} + \varepsilon\partial_x\tau_{xz} + \varepsilon\partial_z\tau_{zz}. \end{cases} \tag{12}$$

We also write the boundary and kinematic conditions using dimensionless variables. At the free surface we get

$$\partial_t h + u_{|_{z=b+h}}\,\partial_x\left(b+h\right) - w_{|_{z=b+h}} = O\left(\varepsilon^2\right); \qquad p_{|_{z=b+h}} = 0, \tag{13}$$

and at the bottom we obtain

$$\begin{aligned} u_{|_{z=b}}\ \partial_x b &= w_{|_{z=b}}; \\ (\eta\partial_z u)_{|_{z=b}} &= \left(\mu(I)p\frac{u}{|u|}\right)_{|_{z=b}} + \mathcal{O}\left(\varepsilon^2\right). \end{aligned} \tag{14}$$

As shown previously, it is convenient to write the set of equations (12) in matrix notation before applying the multilayer approach. First, we focus on the equations of momentum. We multiply the horizontal momentum equation by ε and the vertical one by $1/\varepsilon$. This gives

$$\varepsilon\rho\big(\partial_t u + u\partial_x u + u\partial_z w\big) + \varepsilon\partial_x p = -\rho\frac{1}{Fr^2}\tan\ \theta + \varepsilon^2\partial_x\tau_{xx} + \partial_z\tau_{xz},$$

$$\varepsilon\rho\big(\partial_t w + u\partial_x w + w\partial_z w\big) + \frac{1}{\varepsilon}\partial_z p\ = -\frac{1}{\varepsilon}\rho\frac{1}{Fr^2} + \partial_x\tau_{xz} + \partial_z\tau_{zz}.$$

Note that the stress tensor can be written:

$$\boldsymbol{\tau}_\varepsilon = \eta\, D_\varepsilon(\boldsymbol{u}) \qquad \text{with} \qquad D_\varepsilon(\boldsymbol{u}) := \frac{1}{2}\begin{pmatrix} 2\varepsilon^2\partial_x u & \partial_z u + \varepsilon^2\partial_x w \\ \partial_z u + \varepsilon^2\partial_x w & 2\,\partial_z w \end{pmatrix}. \tag{15}$$

We introduce the notation:

$$\boldsymbol{f} = \left(\frac{\tan\,\theta}{Fr^2},\ \frac{1}{\varepsilon Fr^2}\right)' \qquad \text{and} \qquad \mathcal{E} = \begin{pmatrix} \varepsilon & 0 \\ 0 & 1/\varepsilon \end{pmatrix}.$$

Now we can write the momentum equations as follows

$$\varepsilon\rho\partial_t\boldsymbol{u} + \varepsilon\rho\nabla\cdot(\boldsymbol{u}\otimes\boldsymbol{u}) + \nabla\cdot(p\mathcal{E}) = -\rho\boldsymbol{f} + \nabla\cdot(\eta D_\varepsilon(\boldsymbol{u})),$$

and we obtain the system (12) in matrix notation:

$$\begin{cases} \nabla\cdot\boldsymbol{u} = \ 0, \\ \\ \rho\partial_t\boldsymbol{u} \ + \ \rho\nabla\cdot(\boldsymbol{u}\otimes\boldsymbol{u}) - \dfrac{1}{\varepsilon}\nabla\cdot\boldsymbol{\sigma} \ = \ -\dfrac{1}{\varepsilon}\rho\boldsymbol{f}, \end{cases} \tag{16}$$

where the stress tensor is rewritten as $\boldsymbol{\sigma} = -p\mathcal{E} + \boldsymbol{\tau}_\varepsilon$, with $\boldsymbol{\tau}_\varepsilon$ given by (15).

3.2 A multilayer approach

We apply the multilayer approach introduced in [23] to the system (13)-(16). Note that the structure of the system (16) looks like that of Navier-Stokes equations (1) and then the whole procedure developed in [23] can be followed. In the next lines we describe the main points of the derivation and we introduce the required notation to understand the final model.

3.2.1 Notation

We denote the granular domain $\Omega_F(t)$ and its projection $I_F(t)$ on the reference plane, for a positive $t \in [0,T]$, i.e.

$$I_F(t) = \Big\{x \in \mathbb{R}; (x,z) \in \Omega_F(t)\Big\}.$$

The multilayer approach considers a vertical partition of the domain in $N \in \mathbb{N}^*$ layers with preset thicknesses $h_\alpha(t,x)$ for $\alpha = 1,...,N$, (see figure 1). Note that $\sum_{\alpha=1}^N h_\alpha = h$. In practice, we set a vertical partition of the domain as follows: we introduce the positive coefficients l_α such that

$$h_\alpha = l_\alpha h \quad \text{ for } \alpha = 1,...,N; \qquad \sum_{\alpha=1}^{N} l_\alpha = 1.$$

Note that the thickness of each layer is automatically adapted to the movement of the free surface, since it depends on the total thickness of the mass flow. These layers are separated by $N+1$ interfaces $\Gamma_{\alpha+\frac{1}{2}}(t)$, which are described by the equations $z = z_{\alpha+\frac{1}{2}}(t,x)$ for $\alpha = 0,1,..,N$, $x \in I_F(t)$. We assume that these interfaces are smooth enough. Observe that the fixed bottom and the free surface are respectively $b = z_{\frac{1}{2}}$ and $b+h = z_{N+\frac{1}{2}}$, corresponding to the interfaces at the bottom $\Gamma_{\frac{1}{2}}$ and at the free surface $\Gamma_{N+\frac{1}{2}}$ respectively. Note that $z_{\alpha+\frac{1}{2}} = b + \sum_{\beta=1}^{\alpha} h_\beta$ and $h_\alpha = z_{\alpha+\frac{1}{2}} - z_{\alpha-\frac{1}{2}}$,

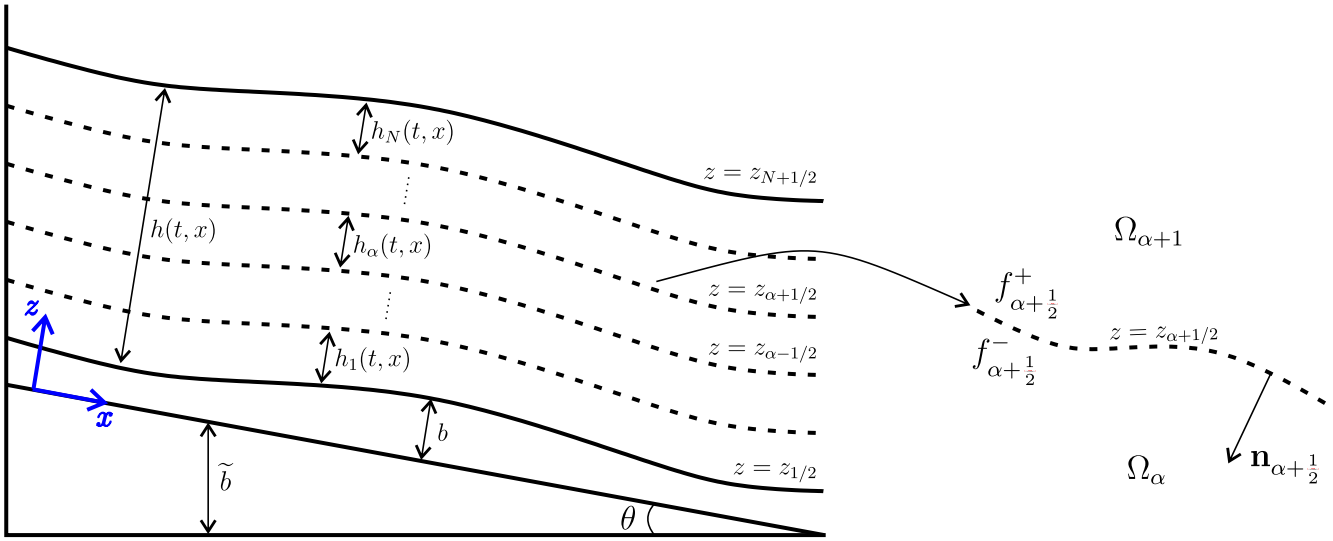

Figure 1: *Sketch of the granular material domain and its multilayer division.*

for $\alpha = 1, ..., N$. The subdomain between $\Gamma_{\alpha-\frac{1}{2}}$ and $\Gamma_{\alpha+\frac{1}{2}}$ is denoted by $\Omega_\alpha(t)$, for a positive $t \in [0, T]$,

$$\Omega_\alpha(t) = \Big\{(x,z);\ x \in I_F(t) \text{ and } z_{\alpha-\frac{1}{2}} < z < z_{\alpha+\frac{1}{2}}\Big\}.$$

We need to introduce a specific notation about the approximations of the variables on the interfaces (see figure 1). For a function f and for $\alpha = 0, 1, ..., N$, we set

$$f^-_{\alpha+\frac{1}{2}} := (f_{|\Omega_\alpha(t)})_{|\Gamma_{\alpha+\frac{1}{2}}(t)} \quad \text{and} \quad f^+_{\alpha+\frac{1}{2}} := (f_{|\Omega_{\alpha+1}(t)})_{|\Gamma_{\alpha+\frac{1}{2}}(t)}.$$

Note that if the function f is continuous,

$$f_{\alpha+\frac{1}{2}} := f_{|\Gamma_{\alpha+\frac{1}{2}}(t)} = f^+_{\alpha+\frac{1}{2}} = f^-_{\alpha+\frac{1}{2}}.$$

In addition, for a given time t, we denote

$$\boldsymbol{n}_{T,\alpha+\frac{1}{2}} = \frac{\Big(\partial_t z_{\alpha+\frac{1}{2}}, \partial_x z_{\alpha+\frac{1}{2}}, -1\Big)'}{\sqrt{1 + \Big(\partial_x z_{\alpha+\frac{1}{2}}\Big)^2 + \Big(\partial_t z_{\alpha+\frac{1}{2}}\Big)^2}} \quad \text{and} \quad \boldsymbol{n}_{\alpha+\frac{1}{2}} = \frac{\Big(\partial_x z_{\alpha+\frac{1}{2}}, -1\Big)'}{\sqrt{1 + \Big(\partial_x z_{\alpha+\frac{1}{2}}\Big)^2}},$$

the space-time unit normal vector and the space unit normal vector to the interface $\Gamma_{\alpha+\frac{1}{2}}(t)$ outward to the layer $\Omega_{\alpha+1}(t)$ for $\alpha = 0, ..., N$.

3.2.2 Weak solution with discontinuities

We are looking for a particular weak solution $(\boldsymbol{u}, p, \rho)$ of (16) (see [23]). We remind the reader that this solution must meet the following conditions:

(i) $(\boldsymbol{u}, p, \rho)$ is a standard weak solution of (16) in each layer $\Omega_\alpha(t)$,

(ii) $(\boldsymbol{u}, p, \rho)$ satisfies the normal flux jump condition for mass and momentum at the interfaces $\Gamma_{\alpha+\frac{1}{2}}(t)$, namely:

$$[(\rho; \rho\boldsymbol{u})]_{\alpha+\frac{1}{2}}\ \boldsymbol{n}_{T,\alpha+\frac{1}{2}} = 0$$

$$\Big[(\rho\boldsymbol{u}; \rho\boldsymbol{u}\otimes\boldsymbol{u} - \frac{1}{\varepsilon}\boldsymbol{\sigma})\Big]_{\alpha+\frac{1}{2}}\ \boldsymbol{n}_{T,\alpha+\frac{1}{2}} = 0$$

where $[(a; b)]_{\alpha+\frac{1}{2}}$ denotes the jump of $(a; b)$ across the interface $\Gamma_{\alpha+\frac{1}{2}}(t)$.

There are two main differences with the derivation in [23]: first, the $\mu(I)$-rheology produces a non-constant viscosity coefficient, which implies an additional difficulty in order to develop the momentum balances at the interfaces. Second, the system to be solved is an asymptotic approximation of the Navier-Stokes equations, which helps to resolve the previous difficulty since we look for a first-order approximation in ε.

A particular family of velocity functions is considered, by assuming that the thickness of each layer is small enough to make the horizontal velocities independent of the vertical variable z (usual shallow domain hypothesis). As a consequence, thanks to the incompressibility condition in each layer, we obtain that vertical velocities are linear in z and maybe discontinuous. We denote the velocity in each layer as

$$\boldsymbol{u}_{|\Omega_\alpha(t)} := \boldsymbol{u}_\alpha := (u_\alpha, w_\alpha)',$$

where u_α and w_α are the horizontal and vertical velocities, respectively, on layer α. Then,

$$\partial_z u_\alpha = 0; \quad \partial_z w_\alpha = d_\alpha(t, x) \tag{17}$$

for some smooth function $d_\alpha(t, x)$.

Pressure

From the asymptotic analysis, we directly get a hydrostatic pressure that is obtained from the vertical momentum equation in (12):

$$\partial_z p_\alpha = -\rho\frac{1}{Fr^2} + \mathcal{O}(\varepsilon).$$

By the continuity of the dynamic pressure, we can deduce at first order that

$$p_\alpha(z) = \frac{\rho}{Fr^2}(b + h - z). \tag{18}$$

Mass conservation across the interfaces and normal velocity

The mass conservation jump condition gives us the definition of the normal mass flux at the interface $\Gamma_{\alpha+\frac{1}{2}}(t)$, denoted by $G_{\alpha+\frac{1}{2}} := G^+_{\alpha+\frac{1}{2}} = G^-_{\alpha+\frac{1}{2}}$ for:

$$G^\pm_{\alpha+\frac{1}{2}} = \partial_t z_{\alpha+\frac{1}{2}} + u^\pm_{\alpha+\frac{1}{2}}\ \partial_x z_{\alpha+\frac{1}{2}} - w^\pm_{\alpha+\frac{1}{2}}. \tag{19}$$

By integrating the incompressibility equation and using this mass conservation condition, we get the definition of the vertical velocity w_α for u_α a solution of (16) (see [23] for details). Thus, if we consider that there is no mass transference with the bottom (i.e. $G_{1/2} = 0$), we obtain

$$w^+_{\frac{1}{2}} = u_1\partial_x b + \partial_t b,$$

and for $\alpha = 1, ..., N$ and $z \in (z_{\alpha-\frac{1}{2}}, z_{\alpha+\frac{1}{2}})$,

$$\left\{ \begin{array}{l} w_\alpha(t,x,z) \;=\; w^+_{\alpha-\frac{1}{2}}(t,x) \;-\; (z - z_{\alpha-\frac{1}{2}})\partial_x u_\alpha(t,x), \\ \\ w^+_{\alpha+\frac{1}{2}} \;=\; (u_{\alpha+1} - u_\alpha)\, \partial_x z_{\alpha+\frac{1}{2}} \;+\; w^-_{\alpha+\frac{1}{2}}; \end{array} \right. \tag{20}$$

where

$$w^-_{\alpha+\frac{1}{2}} = w^+_{\alpha-\frac{1}{2}} - h_\alpha \partial_x u_\alpha.$$

Momentum conservation across the interfaces

The momentum jump conditions become:

$$\frac{1}{\varepsilon}\big[\boldsymbol{\sigma}\big]_{\alpha+\frac{1}{2}} \boldsymbol{n}_{\alpha+\frac{1}{2}} = \frac{\rho\, G_{\alpha+\frac{1}{2}}}{\sqrt{1 + \left|\partial_x z_{\alpha+\frac{1}{2}}\right|^2}}\; [\boldsymbol{u}]_{\alpha+\frac{1}{2}}\,,$$

where, for $\alpha = 1, \dots N-1$, the total stress tensor is

$$\boldsymbol{\sigma}^\pm_{\alpha+\frac{1}{2}} \;=\; -p_{\alpha+\frac{1}{2}}\, \boldsymbol{\mathcal{E}} + \boldsymbol{\tau}^\pm_{\varepsilon,\alpha+\frac{1}{2}},$$

with $p_{\alpha+\frac{1}{2}} = p^+_{\alpha+\frac{1}{2}} = p^-_{\alpha+\frac{1}{2}}$ and $\boldsymbol{\tau}^\pm_{\varepsilon,\alpha+\frac{1}{2}}$ approximations of p_α and $\boldsymbol{\tau}_{\varepsilon,\alpha}$ at $\Gamma_{\alpha+\frac{1}{2}}$. Following [23], we finally get that the momentum jump condition gives

$$\boldsymbol{\tau}^\pm_{\varepsilon,\alpha+\frac{1}{2}}\; \boldsymbol{n}_{\alpha+\frac{1}{2}} = \;\; \widetilde{\boldsymbol{\tau}}_{\varepsilon,\alpha+\frac{1}{2}}\; \boldsymbol{n}_{\alpha+\frac{1}{2}} \pm \frac{1}{2}\frac{\varepsilon\rho G_{\alpha+\frac{1}{2}}}{\sqrt{1 + \left|\partial_x z_{\alpha+\frac{1}{2}}\right|^2}}\; [\boldsymbol{u}]_{|\Gamma_{\alpha+\frac{1}{2}}(t)}\,, \tag{21}$$

where $\widetilde{\boldsymbol{\tau}}_{\varepsilon,\alpha+\frac{1}{2}}$ is an approximation of $\big(\eta D_\varepsilon(\boldsymbol{u}_\alpha)\big)_{|\Gamma_{\alpha+\frac{1}{2}}}$, defined by

$$\widetilde{\boldsymbol{\tau}}_{\varepsilon,\alpha+\frac{1}{2}} = \eta_{\alpha+\frac{1}{2}}\widetilde{D}_{\varepsilon,\alpha+\frac{1}{2}} = \frac{1}{2}\eta_{\alpha+\frac{1}{2}} \begin{pmatrix} 2\varepsilon^2\partial_x\left(\dfrac{u^+_{\alpha+\frac{1}{2}} + u^-_{\alpha+\frac{1}{2}}}{2}\right) & \widetilde{D}_{\varepsilon,\alpha+\frac{1}{2},xz} \\ \\ \left(\widetilde{D}_{\varepsilon,\alpha+\frac{1}{2},xz}\right)' & 2\mathcal{U}^V_{\mathcal{Z},\alpha+\frac{1}{2}} \end{pmatrix}. \tag{22}$$

In this equation,

$$\widetilde{D}_{\varepsilon,\alpha+\frac{1}{2},xz} = \varepsilon^2\partial_x\left(\frac{w^+_{\alpha+\frac{1}{2}} + w^-_{\alpha+\frac{1}{2}}}{2}\right) + \mathcal{U}^H_{\mathcal{Z},\alpha+\frac{1}{2}},$$

and $(\mathcal{U}^H_{\mathcal{Z},\alpha+\frac{1}{2}}, \mathcal{U}^V_{\mathcal{Z},\alpha+\frac{1}{2}})$ is defined to approximate the derivatives in z. We remind the reader that we use a mixed formulation because of the possible vertical discontinuous profile. Thus, the auxiliary unknown $\mathcal{U}_\mathcal{Z}$ satisfies

$$\mathcal{U}_\mathcal{Z} - \partial_z \boldsymbol{u} = 0, \quad \text{with} \quad \mathcal{U}_\mathcal{Z} = (\mathcal{U}^H_\mathcal{Z}, \mathcal{U}^V_\mathcal{Z}). \tag{23}$$

And to approximate $\mathcal{U}_{\mathcal{Z}}$, we approximate $\boldsymbol{u}$ by $\widetilde{\boldsymbol{u}}$, a $\mathbb{P}_1(z)$ interpolation such that $\widetilde{\boldsymbol{u}}_{|z=\frac{1}{2}(z_{\alpha-\frac{1}{2}}+z_{\alpha+\frac{1}{2}})} = \boldsymbol{u}_\alpha$. Then $\mathcal{U}_{\mathcal{Z}\,\alpha+\frac{1}{2}} = \left(\mathcal{U}^H_{\mathcal{Z}\,,\alpha+\frac{1}{2}}, \mathcal{U}^V_{\mathcal{Z}\,,\alpha+\frac{1}{2}}\right)$ is an approximation of $\mathcal{U}_{\mathcal{Z}}(\widetilde{\boldsymbol{u}})$ at $\Gamma_{\alpha+\frac{1}{2}}$.

Let us remark that the previous expression of the tensor $\widetilde{\boldsymbol{\tau}}_{\varepsilon,\alpha+\frac{1}{2}}$ in (22) has the same structure as the original case in [23], except for the viscosity that now is not constant because it is defined by the $\mu(I)$-rheology in (6). Then, we must give an approximation of the viscosity at the interface up to first order in ε, which we denoted by $\eta_{\alpha+\frac{1}{2}}$. We have considered the following first-order approximation of $\|D(\boldsymbol{u})\|$ at $z = z_{\alpha+\frac{1}{2}}$,

$$\|D(\boldsymbol{u})\|_{\alpha+\frac{1}{2}} \approx \left|\mathcal{U}^H_{\mathcal{Z}\,,\alpha+\frac{1}{2}}\right|. \tag{24}$$

Then, it reads

$$\eta_{\alpha+\frac{1}{2}} = \eta_{\alpha+\frac{1}{2}}(\mathcal{U}^H_{\mathcal{Z}\,,\alpha+\frac{1}{2}}) = \frac{\mu(I_{\alpha+\frac{1}{2}})p_{\alpha+\frac{1}{2}}}{\max\left(\left|\mathcal{U}^H_{\mathcal{Z}\,,\alpha+\frac{1}{2}}\right|, \frac{\mu(I_{\alpha+\frac{1}{2}})p_{\alpha+\frac{1}{2}}}{\eta_M}\right)}, \tag{25}$$

with

$$\mathcal{U}^H_{\mathcal{Z}\,,\alpha+\frac{1}{2}} = \frac{u_{\alpha+1}-u_\alpha}{h_{\alpha+\frac{1}{2}}}, \qquad \text{for} \quad \alpha = 1,\dots,N-1,$$

with $h_{\alpha+\frac{1}{2}}$ being the distance between the midpoints of layers α and $\alpha+1$. Moreover,

$$\mathcal{U}^H_{\mathcal{Z}\,,\frac{1}{2}} = \frac{u_1}{h_1},$$

and

$$p_{\alpha+\frac{1}{2}} = \frac{\rho}{Fr^2}\sum_{\beta=\alpha+1}^{N} h_\beta\,, \qquad I_{\alpha+\frac{1}{2}} = \frac{2\,d_s\left|\mathcal{U}^H_{\mathcal{Z}\,,\alpha+\frac{1}{2}}\right|}{\sqrt{p_{\alpha+\frac{1}{2}}/\rho_s}}, \quad \text{for} \quad \alpha = 0,\dots,N-1. \tag{26}$$

Note that $\eta_{N+1/2} = 0$, because we suppose that the atmospheric pressure is zero.

3.3 Final model

The final model is derived as in [23] by looking for a particular weak solution of the asymptotic system (16). First the equations (16) are multiplied by some test functions, and secondly we integrate this system in the domain $\Omega_\alpha(t)$ (see Appendix A for more details). In this way, the final $\mu(I)$-rheology multilayer model is obtained in dimensionless variables. The last step is to come back to the original variables taking into account the assumptions described in Subsection 3.1. As a result, the final model reads, for $\alpha = 1, ..., N$,

$$\begin{cases} l_\alpha\Big(\partial_t h + \partial_x(hu_\alpha)\Big) = G_{\alpha+\frac{1}{2}} - G_{\alpha-\frac{1}{2}}, \\ l_\alpha\Big(\rho\partial_t\left(hu_\alpha\right) \;+\; \rho\partial_x\left(hu_\alpha^2\right) + \rho g\;\cos\theta\, h\,\partial_x\left(b+\tilde{b}+h\right)\Big) \;= \\ \quad = \; K_{\alpha-\frac{1}{2}} - K_{\alpha+\frac{1}{2}} \;+\; \dfrac{1}{2}\rho G_{\alpha+\frac{1}{2}}\left(u_{\alpha+1}+u_\alpha\right) \;-\; \dfrac{1}{2}\rho G_{\alpha-\frac{1}{2}}\left(u_\alpha+u_{\alpha-1}\right) \end{cases} \tag{27}$$

where $G_{\alpha+\frac{1}{2}}$ are given in (19),

$$K_{\alpha+\frac{1}{2}} = -\eta_{\alpha+\frac{1}{2}}(\mathcal{U}^H_{\mathcal{Z},\alpha+\frac{1}{2}})\,\mathcal{U}^H_{\mathcal{Z},\alpha+\frac{1}{2}} \qquad \text{and} \qquad K_{\frac{1}{2}} = -\mu\big(I_{\frac{1}{2}}\big)\rho g\,\cos\theta\, h\frac{u_1}{|u_1|}, \tag{28}$$

for $\eta_{\alpha+\frac{1}{2}}$ defined in (25)-(26).

Note that the proposed model (27) has $2N$ equations and unknowns:
$(h, \{hu_\alpha\}_{\alpha=1,\dots,N}, \{G_{\alpha+\frac{1}{2}}\}_{\alpha=1,\dots,N-1})$. But thanks to (19)-(20) we can write

$$G_{\alpha+\frac{1}{2}} = \partial_t z_{\alpha+\frac{1}{2}} + \frac{u_\alpha + u_{\alpha+1}}{2}\partial_x z_{\alpha+\frac{1}{2}} - w_{\alpha+\frac{1}{2}}, \quad \text{where} \quad w_{\alpha+\frac{1}{2}} = \frac{w^+_{\alpha+\frac{1}{2}} + w^-_{\alpha+\frac{1}{2}}}{2}.$$

As a consequence, the system has $2N$ unknowns that are also the total height (h), the discharge at each layer ($\{hu_\alpha\}_{\alpha=1,\dots,N}$) and the averaged vertical velocity at each internal interface ($\{w_{\alpha+\frac{1}{2}}\}_{\alpha=1,\dots,N-1}$).

Nevertheless, by combining the continuity equations, the system can be rewritten with $N+1$ equations and unknowns. The unknowns of the reduced system are the total height (h) and the discharge of each layer,

$$q_\alpha = h\,u_\alpha, \quad \text{for} \quad \alpha = 1,\dots,N.$$

By introducing (see [23])

$$\xi_{\alpha,\gamma} = \begin{cases} \big(1 - (l_1 + \cdots + l_\alpha)\big)l_\gamma, & \text{if } \gamma \le \alpha, \\ \\ -(l_1 + \cdots + l_\alpha)l_\gamma, & \text{otherwise,} \end{cases}$$

for $\alpha,\ \gamma \in \{1,\dots,N\}$, the system (27)-(28) is rewritten as

$$\begin{cases} \partial_t h + \partial_x\left(\displaystyle\sum_{\beta=1}^{N} l_\beta q_\beta\right) = 0, \\ \\ \partial_t q_\alpha + \partial_x\left(\dfrac{q_\alpha^2}{h} + g\,\cos\theta\dfrac{h^2}{2}\right) + g\,\cos\theta\, h\,\partial_x z_b + \\ \quad + \displaystyle\sum_{\gamma=1}^{N}\frac{1}{2hl_\alpha}\Big((q_\alpha + q_{\alpha-1})\,\xi_{\alpha-1,\gamma} - (q_{\alpha+1} + q_\alpha)\,\xi_{\alpha,\gamma}\Big)\partial_x q_\gamma \ = \\ \quad = \dfrac{1}{\rho l_\alpha}\Big(\vec{K}_{\alpha-\frac{1}{2}} - \vec{K}_{\alpha+\frac{1}{2}}\Big) \qquad\qquad \alpha = 1,\dots,N, \end{cases}$$

where $z_b = b + \tilde{b}$ has been introduced for simplicity.

Moreover, we can see that this model satisfies a dissipative energy inequality. Denoting the energy of the layer $\alpha = 1, \cdots, N$ for the system (27)-(28) by

$$E_\alpha = h_\alpha\left(\frac{|u_\alpha|^2}{2} + g\,\cos\theta\,\left(z_b + \frac{h}{2}\right)\right),$$

the following dissipative energy inequality is satisfied:

$$\rho\partial_t\left(\sum_{\alpha=1}^{N} E_\alpha\right)+\rho\partial_x\left[\sum_{\alpha=1}^{N} u_\alpha\left(E_\alpha+\rho g\,\cos\theta\, h_\alpha\frac{h}{2}\right)\right]\leq$$

$$\leq -\rho g\,\cos\theta\, h\,|u_1|\,\mu(I)-\frac{|u_N|^2}{h_N}\eta_{N+\frac{1}{2}}-\sum_{\alpha=1}^{N-1}\frac{(u_{\alpha+1}-u_\alpha)^2}{h_{\alpha+\frac{1}{2}}}\eta_{\alpha+\frac{1}{2}}.$$

Finally, note that if we consider a no-slip condition to deduce the model instead of the Coulomb friction condition (10), the only difference that appears in the multilayer approach is the definition of $K_{\frac{1}{2}}$. It must be defined directly in terms of the rheology, in the same way as $K_{\alpha+\frac{1}{2}}$ for $\alpha=1,\ldots,N-1$. That is,

$$K_{\frac{1}{2}}=-\eta_{\frac{1}{2}}(\mathcal{U}^H_{\mathcal{Z},\frac{1}{2}})\,\mathcal{U}^H_{\mathcal{Z},\frac{1}{2}},$$

where $\mathcal{U}^H_{\mathcal{Z},\frac{1}{2}}$ is an approximation of the horizontal component of the solution of equation (23) for $z=b$. Then, using the no-slip condition, a second-order approximation is

$$\mathcal{U}^H_{\mathcal{Z},\frac{1}{2}}=\frac{2\,u_1}{h_1}.$$

4 Numerical tests

The numerical approximation is performed in 2D (downslope and normal directions). We rewrite the model as a non-conservative hyperbolic system with source terms as in [23]. Then a splitting procedure is considered.
First, we set aside the term that appears in the internal interfaces and a standard path-conservative finite volume method is applied. These path-conservative methods were introduced in [41]. To deal with the Coulomb friction term, we use the hydrostatic reconstruction introduced in [2], which is applied in [11] to solve the Saint-Venant system with Coulomb friction. The main advantage of this reconstruction is its great stability.
The second step is to solve the contribution of the term in the internal interfaces, which represents the mass and momentum exchange between layers. In this step, a semi-implicit scheme is employed, taking into account the regularization of $\|D(\boldsymbol{u}_\alpha)\|$ mentioned in Section 2.2 in order to avoid the singularity when $\|D(\boldsymbol{u}_\alpha)\|$ vanishes.

In order to validate the Multilayer Shallow Model (denoted MSM hereafter) with the $\mu(I)$-rheology, we compare it to (i) 2D steady and transient uniform flows over inclined surfaces with and without the effect of sidewall friction (analytical solutions and experimental data for deep and surface flows), (ii) laboratory experiments of highly transient and non-uniform granular flows over inclined planes covered by an erodible bed, in which case the shape of the velocity profiles strongly changes with time and space.

4.1 Granular surface flows in channel

In this subsection we deal with several Bagnold flows. First, we consider a uniform Bagnold flow without taking into account the effect of the lateral wall friction. Then, we show that our multilayer model is able to capture the velocity profiles for flows in a narrow channel when sidewall friction

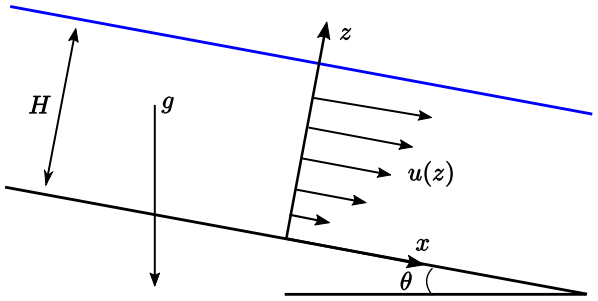

Figure 2: *Sketch of the analytical solution.*

is introduced. In that case we compare with the analytical solution and laboratory experiments. Note that Bagnold flows verify, at the free surface

$$p_{|z=H} = 0 \qquad \text{and} \qquad \|D(u)\|_{|z=H} = |\partial_z u|_{|z=H} = 0.$$

Therefore, we cannot use the regularization (6) since its denominator vanishes at the free surface. In this case we use the regularization

$$\eta = \frac{\mu(I)p}{\sqrt{\|D(\boldsymbol{u})\|^2 + \delta^2}},$$

where $\delta > 0$ is a small parameter (see [8]).

4.1.1 Steady uniform Bagnold flow: analytical solution

Let us first compare the model with the analytical solution for a uniform flow over an inclined plane of slope θ and thickness $H > 0$, i.e. a Bagnold flow (see [24], [49] or [34]). This solution is obtained by imposing zero pressure and zero shear stress at the free surface and a no-slip condition at the bottom (Coulomb friction can be easily changed by no-slip condition in the $\mu(I)$-rheology multilayer model, see Sections 2.3 and 3.3).

By denoting u and w the downslope and normal velocities, p the pressure and τ the shear stress and by taking the rheological parameters defined in Section 2.2, the steady uniform Bagnold flow is described by

$$\begin{cases} u(z) = \dfrac{2}{3d_s} I_0 \left(\dfrac{\tan\theta - \mu_s}{\mu_2 - \tan\theta} \right) \sqrt{\varphi_s g \cos\theta} \left(H^{3/2} - (H-z)^{3/2} \right), \\ u(z=0) = 0, \quad w = 0, \\ p(z) = \rho g \cos\theta \, (H - z), \\ \tau(z) = \mu(I)p = \rho g \sin\theta \, (H - z), \\ p(z=H) = 0, \quad \tau(z=H) = 0, \\ \mu(I) = \tan(\theta), \qquad\qquad \text{for } z \in (0, H). \end{cases} \tag{29}$$

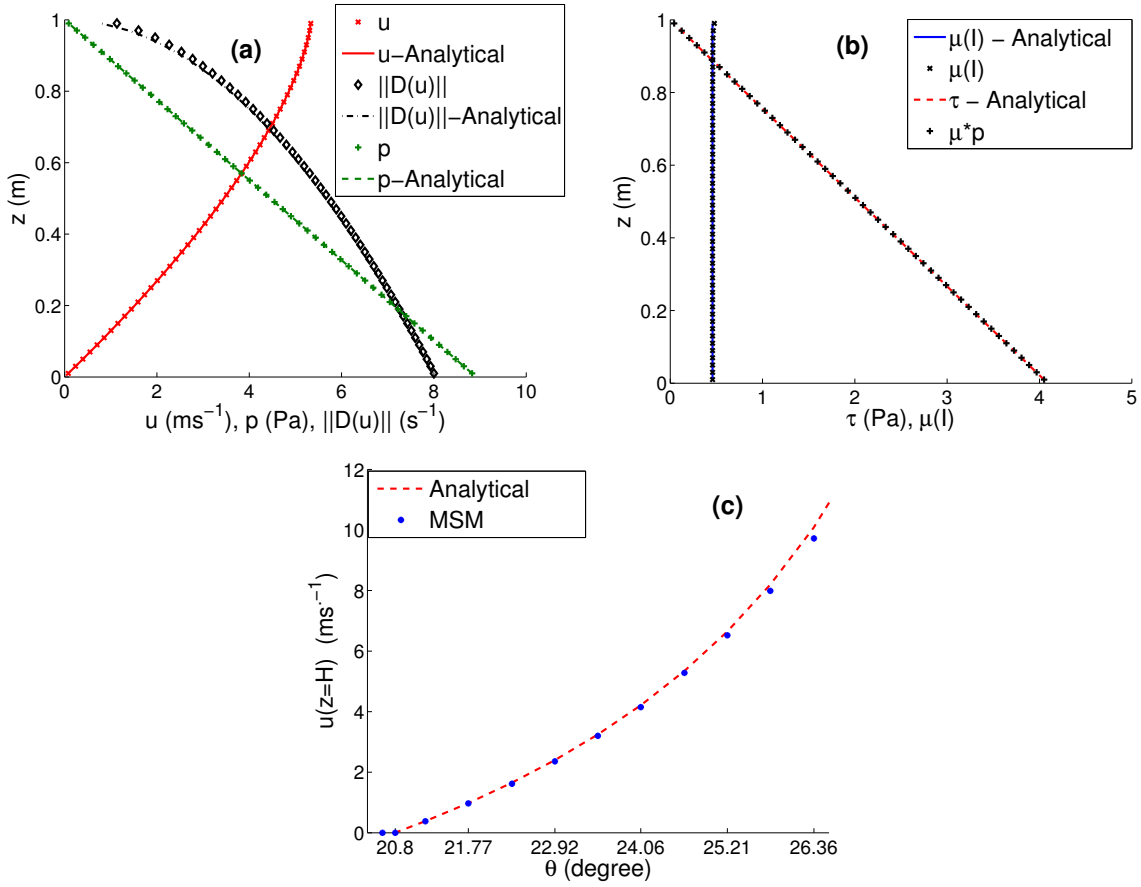

Figure 3: *Comparison between the analytical solution (dashed and solid lines) and the simulations obtained using the MSM with the $\mu(I)$-rheology (symbols). (a) Analytical and simulated downslope horizontal velocity u, pressure p and strain rate $\|D(\boldsymbol{u})\|$; (b) Analytical and simulated shear stress and friction coefficient $\mu(I)$; (c) Comparison between the simulated (symbols) and the exact (dashed line) horizontal velocity at the free surface as a function of the slope angle.*

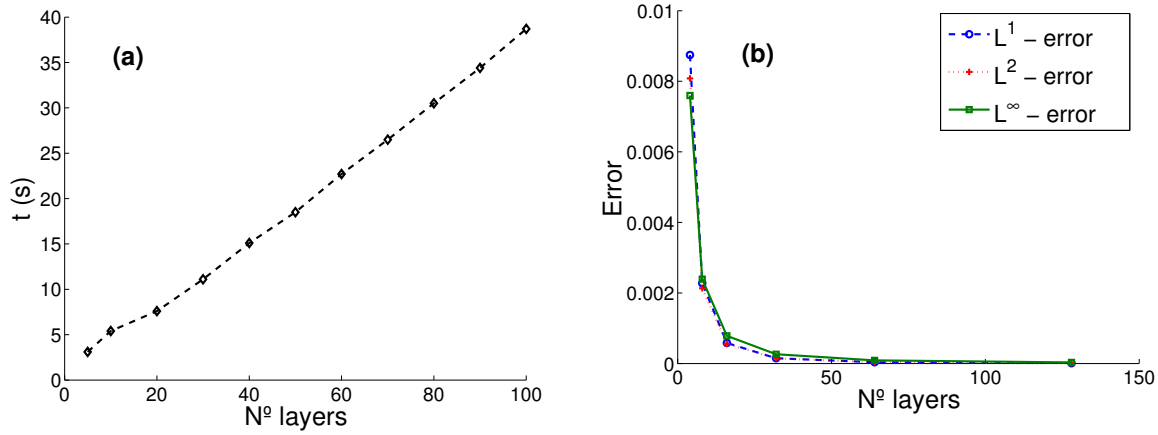

Figure 4: *(a) Computing time as a function of the number of layers in the MSM and (b) relative error between the computed and exact velocity for simulations over a slope of $\theta = 24.64°$.*

$N(\Delta z = 1/N)$	L^1 - Error	L^1 - Order	L^2 - Error	L^2 - Order	L^∞ - Error	L^∞ - Order
4	8.74e-3	–	8.08e-3	–	7.59e-3	–
8	2.27e-03	1.84	2.13e-3	1.92	2.39e-3	1.66
16	5.84e-04	1.96	5.58e-4	1.93	7.84e-4	1.61
32	1.48e-04	1.97	1.45e-4	1.941	2.62e-4	1.57
64	3.76e-05	1.982	3.76e-5	1.948	8.94e-5	1.55
128	9.48e-06	1.988	9.73e-6	1.95	3.08e-5	1.53

Table 1: *Order of the error for the velocity of the Bagnold flow.*

For the numerical simulation, as in the analytical solution, we consider a uniform flow with constant thickness $H = 1$ m and velocity $u = w = 0$ m$\cdot$ s^{-1} at the initial time $t = 0$ s. The boundary conditions at the free surface and at the bottom have been set as in (29). At the right and left boundaries, we use open boundary conditions.

We choose the rheological parameters $I_0 = 0.279$ and $\mu_s = 0.38 \approx \tan(20.8°)$, $\mu_2 = 0.62 \approx \tan(31.8°)$ and the particle diameter $d_s = 4$ cm with solid volume fraction $\varphi_s = 0.62$. The slope angle is taken as $\theta = 0.43$ rad $\approx 24.64°$. Figure 3 shows the good agreement between the simulated and exact solutions for the profiles of the velocity, pressure, shear stress, $\mu(I)$ and $\|D(u)\|$. It also shows the downslope velocity at the free surface as a function of the slope angle. Note that for slopes smaller than $\arctan(\mu_s)$, the surface velocity is close to zero (it is not equal to zero, because of the regularization method), namely $u(z = H) \sim 10^{-5}$, so that the mass is almost at rest.

These results are computed using 50 layers in the MSM. Note that we use a slope in the well-posed region described in [7] for the full $\mu(I)$-rheology, which is smaller than the well-posed region for the depth-averaged $\mu(I)$-rheology (well-posed for $\delta_s = 20.8^o \leqslant \theta < \delta_2 = 31.8^o$ in the case of depth-averaged $\mu(I)$-rheology). If we use a slope close enough to δ_2 the system becomes unstable because of the ill-posedness of the full $\mu(I)$-rheology in this region.

Figure 4 shows the computing time required to simulate 50 seconds (on a laptop with Intel®Core™ i7-4500U and 8 GB of RAM) and the relative error between the computed velocity and the exact solution using a different number of layers and 30 nodes in the x-direction. In table 1 we show that second-order accuracy is reached in norms L^1 and L^2, while in norm L^∞ the order is over 1.5. This behaviour in norm L^∞ is due to the boundary conditions at the free surface, where the analytical solution verifies that $\partial_z u = 0$.

4.1.2 2D steady uniform flow in a channel: sidewalls effect on the velocity profile

The relevance of the lateral wall friction when a granular material flows in a channel has been proved by Jop *et al.* [31] (see also [6]). Under the hypothesis of a steady uniform flow and neglecting the variations in the transverse direction, they propose to model this effect with a modified $\mu(I)$-rheology by adding an extra term, which defines an effective friction term

$$\mu(I) = \mu_s + \frac{\mu_2 - \mu_s}{I_0 + I} I + \mu_w \frac{H - z}{W}, \tag{30}$$

where W is the channel width, μ_w is the constant coefficient of friction with the side walls and H the thickness of the flow. Note that this extra term (last term) increases when we get closer to the bottom from the free surface. In addition, for a channel slope θ with respect to the horizontal

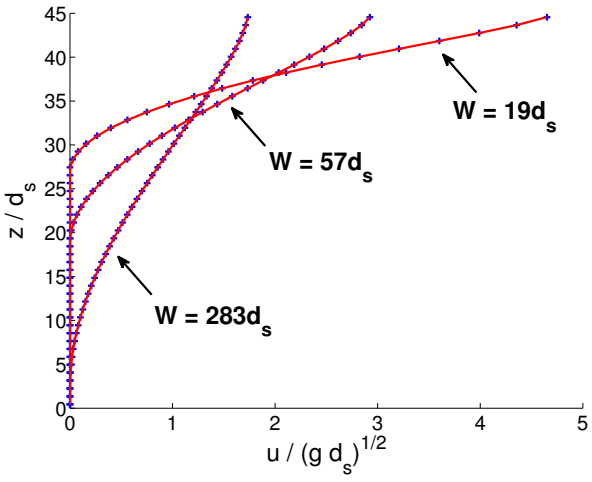

Figure 5: *Comparison between the analytical solution (solid lines) and the simulations obtained using the MSM with the $\mu(I)$-rheology (symbols) for the velocity profile for $Q^* = 31.5$, and different widths: $W = 19d_s$, $W = 57d_s$ and $W = 283d_s$.*

axis, the analytical expression for the velocity profile reads (see appendix B in [31]):

$$u(z) = 2\,\frac{I_0\sqrt{\varphi_s\; g\;\cos\;\theta}}{d_s}\left[\frac{1}{3}\,(H-z)^{3/2} - \frac{1}{3}\,(H-h^*)^{3/2}\;-\right.$$
$$-\frac{\mu_2-\mu_s}{\mu_w}W\left((H-z)^{1/2}\;-\;(H-h^*)^{1/2}\right)\;+$$
$$\left.+\;\sqrt{h_2}\;\frac{\mu_2-\mu_s}{\mu_w}W\left(\arctan\sqrt{\frac{H-z}{h_2}}\;-\;\arctan\sqrt{\frac{H-h^*}{h_2}}\right)\right],$$

where

$$h^* = H - \frac{\tan\;\theta-\mu_s}{\mu_w}\,W, \qquad h_2 = \frac{\mu_2-\tan\;\theta}{\mu_w}\,W.$$

Note that we can integrate the last equation and the discharge is obtained as a function of the slope θ. In these experiments, Jop *et al.* [31] fixed the discharge and computed the velocity profile for different widths. We choose the same material and rheological properties and perform these experiments. The grain diameter is $d_s = 0.53$ mm and the volume fraction is $\varphi_s = 0.6$. The rheological parameters are $\mu_s = \tan(20.9^o)$, $\mu_2 = \tan(32.76^o)$ and $I_0 = 0.279$. The friction coefficient with the sidewalls is $\mu_w = \tan(10.4^o)$. We set the thickness of the flow $H = 45d_s$, the dimensionless discharge $Q^* = 31.5$ and different widths of the channel are considered ($W = 19d_s$, $57d_s$, $283d_s$).

Figure 5 shows the exact agreement between the analytical solution and the simulations for the velocity profile. In this case we consider 50 layers to obtain the solution. In table 2 we present the errors and accuracy order of the method for $W = 283d_s$. We obtain similar results to those presented in the previous subsection.

4.1.3 Laboratory experiments: transient velocity profiles

We compare our model with the experiments and simulations presented in [33] where granular material is flowing within a narrow channel of width $W = 19d_s \approx 1$ cm. The grain diameter is

$N(\Delta z = 1/N)$	L^1 - Error	L^1 - Order	L^2 - Error	L^2 - Order	L^∞ - Error	L^∞ - Order
4	1.72e-2	–	1.41e-2	–	1.14e-2	–
8	4.71e-3	1.87	5.24e-3	1.43	6.61e-3	0.78
16	1.33e-3	1.82	1.21e-3	2.11	1.42e-3	2.21
32	2.65e-4	2.32	3.50e-4	1.79	7.23e-4	0.97
64	7.46e-5	1.83	1.00e-4	1.80	2.56e-4	1.49
128	1.80e-5	2.05	2.58e-5	1.95	8.80e-5	1.54

Table 2: *Order of the error for the velocity of the Bagnold flow with lateral wall effect. Case* $W = 283\, d_s$.

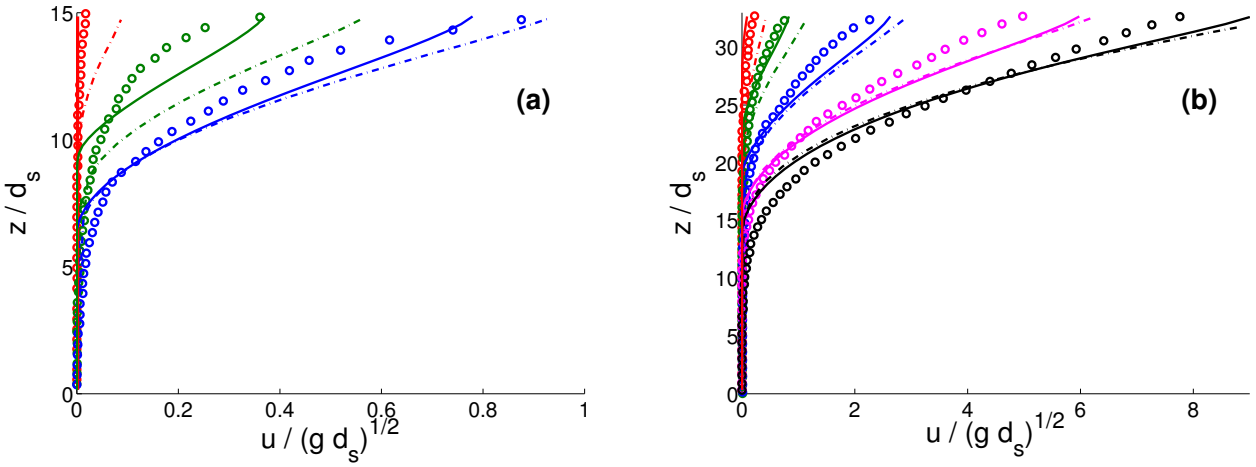

Figure 6: *Comparison between the laboratory experiments (symbols) and simulations (dash-dotted lines) in [33], and simulations using the MSM with the* $\mu(I)$*-rheology (solid lines) for the transient velocity profiles for two different slopes* θ*, and times* $t^* = t/\sqrt{d_s/g}$ *: (a)* $\theta = 26.1^o$*,* $t^* = 1.2, 15.1, 166.1$*; (b)* $\theta = 32.15^o$*,* $t^* = 2.3, 7.5, 24.2, 77.8, 175$.

$d_s = 0.53$ mm, the volume fraction is $\varphi_s = 0.6$ and the rheological parameters are $\mu_s = \tan(20.9^o)$, $\mu_2 = \tan(32.76^o)$ and $I_0 = 0.279$. The friction with the wall is modelled as in the precedent test, following (30). In this case, the authors set the friction coefficient with the sidewalls as $\mu_w = \tan(13.1^o)$.

For the simulations, we impose zero velocity at the initial time and the material flows because of the gravitational force. We use 50 layers in the MSM. Figure 6 shows the comparison between the results in [33] and the simulation using the MSM $\mu(I)$-rheology model for the transient velocity profiles and its final state in two configurations. As is concluded in [33], the agreement for the transient velocity profiles is better for high slopes and less accurate for low inclinations. In the case of high inclination angles our model results are similar to their simulations (see figure 6b), and are slightly better in the other cases (see figure 6a).

4.2 Granular collapse experiments

We will now use the MSM to simulate the laboratory experiments performed in [38]. The objectives are: to evaluate if (i) the model with the $\mu(I)$-rheology gives a reasonable approximation of the flow dynamics and deposits of highly transient and non-uniform granular flows, (ii) it recovers the strong change in the shape of the velocity profiles with time and space, (iii) it reproduces the increase in runout distance observed for increasing thickness of the erodible bed above a critical

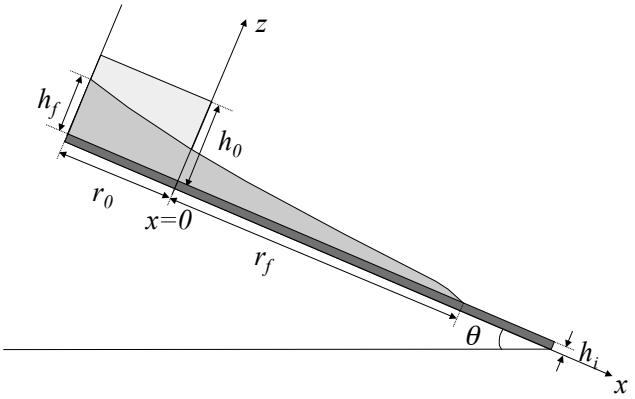

Figure 7: *Sketch of the initial and final state of the granular collapse. A granular column with a thickness $h_0 = 14$ cm and a length $r_0 = 20$ cm is released on an inclined plane of slope θ. The plane is covered by an erodible bed of thickness h_i made of the same material. When the flow stops, the maximum final thickness is h_f and its final extent r_f.*

slope angle $\theta_c \in [12^o, 16^o]$ and (iv) the multilayer approach improves the results compared to the classical depth-averaged Saint-Venant model (i.e. monolayer model).

In Subsection 4.2.1 we also introduce a modification in the calculation of the friction coefficient $\mu(I)$. In particular, we take into account second-order terms to approximate $\|D(\boldsymbol{u})\|$. As shown below, this correction provides better results in some test cases.

4.2.1 Improvement of the approximation of the $\mu(I)$ coefficient

The advantage of the multilayer models is that we obtain a variable profile of the downslope velocity, in contrast with the prescribed profile of the monolayer model. It makes it possible to obtain a better approximation of $\|D(\boldsymbol{u})\|$ (see equation (24)). As a consequence, this improves the approximation of the inertial number I (see equations (4) and (26)), which is a key number in the variable friction coefficient $\mu(I)$.

As the main advantage of the multilayer model is the improvement of the approximation of $\|D(\boldsymbol{u})\|$, we present two approximations that can be made with the multilayer model. First, let us recall that a first-order approximation corresponds to the definition (24). This approximation considers only the leading-order term, i.e. $\|D(\boldsymbol{u})\|_{\alpha+\frac{1}{2}} \approx \left|\partial_z u_{\alpha+\frac{1}{2}}\right| = \left|\mathcal{U}^H_{\mathcal{Z},\alpha+\frac{1}{2}}\right|$. Note that in dimensionless form, we have

$$\|D(\boldsymbol{u})\| = \sqrt{\frac{1}{\varepsilon^2}\left(\partial_z u\right)^2 + 4\left(\partial_x u\right)^2 + 2\partial_x w \partial_z u + \varepsilon^2\left(\partial_x w\right)^2}. \tag{31}$$

We can improve the approximation of $\|D(\boldsymbol{u})\|$ at the interfaces $z = z_{\alpha+\frac{1}{2}}$ by considering the approximation taking into account second-order terms in the previous equation. For the numerical tests, we consider the following approximation $\|D(\boldsymbol{u})\|$ at the interfaces,

$$\|D(\boldsymbol{u})\|_{\alpha+\frac{1}{2}} \approx \sqrt{\left|\mathcal{U}^H_{\mathcal{Z},\alpha+\frac{1}{2}}\right|^2 + \left(\partial_x(u_{\alpha+1} + u_\alpha)\right)^2}. \tag{32}$$

Note that this definition corresponds to an approximation of

$$\|D(\boldsymbol{u})\| \approx \sqrt{(\partial_z u)^2 + 4\,(\partial_x u)^2}$$

at $z = z_{\alpha+\frac{1}{2}}$. Nevertheless, in (31), the term $2\partial_z u\,\partial_x w$ is not taken into account although it is of the same order as $4(\partial_x u)^2$. This is because when an approximation of this term is added, we obtain results that are very similar to those obtained when considering (32). Furthermore adding this term implies an additional computational cost since pre-calculated vertical velocities are required. Note that (32) is a second-order correction while we have developed a first-order model that neglects other second-order terms. This correction, however, highlights the importance of second-order terms in granular collapses over erodible beds, even if it is a partial correction.

The effect of this second-order approximation on the results is discussed below in Sections 4.2.3 and 4.2.4. In particular, we observe an improvement of the results compared to the original first-order approximation of $\|D(\boldsymbol{u})\|$.

4.2.2 Experimental and test data

In the laboratory experiments performed in [38], subspherical glass beads of diameter $d_s = 0.7$ mm were used. The particle density $\rho_s = 2500$ kg m^{-3} and volume fraction $\varphi_s = 0.62$ were estimated, leading to an apparent flow density $\rho = \varphi_s \rho_s = 1550$ kg m^{-3}.
The variable r_f denotes the runout distance, i.e. the length of the deposit measured from the position of the front of the released material at the initial time located at $x = 0$ m, t_f denotes the flow time from $t = 0$ s to the time when the material stops and h_f denotes the maximum final thickness of the deposit (see figure 7).

In order to use the $\mu(I)$-rheology, the rheological parameters (μ_s, μ_2 and I_0) must be defined. We consider the data proposed in [28]. The minimum and maximum friction angles are $\mu_s = \tan(20.9^o)$ and $\mu_2 = \tan(32.76^o)$, according to the measurements made in the experiments presented in [45] and [31]. These parameters can be obtained by fitting the curve $h_{stop}(\theta)$, where h_{stop} is the thickness of the deposit lying on the slope when the supply is stopped after steady uniform flow (see [44] for more details). Nevertheless, in [28] the value of μ_s and μ_2 are incremented, in order to consider the effect of lateral wall friction. Let us remember that lateral wall friction is modelled in [31] as an additional friction term $\mu_w(h - z)/W$, where $\mu_w = \tan(10.4^o)$ is the coefficient of friction in the side walls. Moreover, the thickness of the flowing layer (see [38]) is approximately 0.05 m and the width of the channel $W = 10$ cm. Therefore, the additional friction term is approximately 0.1. As a result, in [28] the authors propose to consider $\mu_s = \tan(25.5^\circ) \approx \tan(20.9^o) + 0.1$ and $\mu_2 = \tan(36.5^\circ) \approx \tan(32.76^o) + 0.1$. Moreover, we set $I_0 = 0.279$ (see [32]).

That might be a coarse way to introduce the wall friction effect, owing that the multilayer model is able to approximate the term $\mu_w(h - z)/W$ in each layer. However, introducing the friction term $\mu_w(h - z)/W$ does not give good results in this granular collapse test. Actually it seems that there is not enough friction at the initial times to well capture the S-shaped profile. Note that the numerical simulations with the proposed hydrostatic multilayer approach cannot be accurate at short times because the dominant effect is the non-hydrostatic pressure. At short times the flowing layer can be overestimated, and, consequently, the effect of the lateral wall friction is not properly taken into account. These comparisons only make sense at the latter stage of the flow. We plot the results for intermediate times in order to illustrate this discussion (see figure 15).

This experiment has been simulated for different slopes θ and thicknesses h_i of the erodible bed: $\theta = 16^\circ$ and $h_i = 1.4,\ 2.5,\ 5$ mm, $\theta = 19^\circ$ and $h_i = 1.5,\ 2.7,\ 5.3$ mm, $\theta = 22^\circ$ and

Models/Data	Acronyms	Line style
Experimental data	Lab	
Multilayer Shallow Model	$\mu(I)$ - MSM	
MSM with the correction (32)	$\mu(I)$ - C - MSM	
Monolayer Model	$\mu(I)$ - monolayer	
MSM with const. friction coef.	μ_s - MSM	
Monolayer Model with const. friction coef.	μ_s - monolayer	

Table 3: *Summary of notation of the different models and colors-symbols*

$h_i = 1.82,\ 3.38,\ 4.6$ mm, and $\theta = 23.7°$ and $h_i = 1.5,\ 2.5,\ 5$ mm. Note that the model does not take into account the effect of removing the gate during the initial instants even though it has a non-negligible impact on the flow dynamics as shown in [28]. For instance, when the gate is taken into account, even with no friction along it, the flow is substantially slowed down; however, the deposit is almost unchanged. All the simulations are performed using 20 layers.

We compare hereafter (i) the constant and variable friction rheologies and (ii) the monolayer and multilayer approaches. In table 3, we summarize the notation and symbols used for the different models. MSM is the notation for multilayer models. Note that the monolayer model with a constant friction coefficient (denoted μ_s-monolayer model) corresponds to the Savage-Hutter classical model when $K_{act/pas} = 1$. This model is widely used in the literature, e.g. [27], [39]. Note also that the monolayer model with a variable friction coefficient (denoted $\mu(I)$-monoloyer model) corresponds to the one proposed by Pouliquen [44], which has been recently used by Mangeney-Castelnau *et al.* [40] and Mangeney *et al.* [37]. This model also coincides with the one proposed in [26] by dropping second-order terms, that is, viscous terms.

4.2.3 Deposit profiles

Let us compare the deposits simulated with the $\mu(I)$-rheology and with a constant friction coefficient μ_s for different slopes θ and erodible bed thicknesses h_i. Figure 8 shows that the deposit calculated with the variable friction coefficient $\mu(I)$ is closer to the experimental deposit than the one calculated with a constant friction coefficient μ_s. The runout distance with the constant coefficient μ_s is always too long except for $\theta = 19^o$ and $h_i = 5.3$ mm (see figure 8d). To properly reproduce the runout distance with a constant friction coefficient, we need to increase its value. For example, with a slope $\theta = 16°$ and an erodible bed thickness $h_i = 2.5$ mm (figure 8a), we need to use the value $\mu_s = \tan(27.3°)$ to produce the runout observed in the laboratory experiments. That means an increment of 0.039 in the μ_s value. These results are consistent with the simulations of [28], showing that the runout is strongly overestimated when the viscosity tends to zero (i. e. when μ tends to μ_s).

Figure 9 shows, for a slope $\theta = 22°$ and $h_i = 1.82$ mm, the final deposit obtained using the constant or variable friction coefficients for multilayer and monolayer models. The difference between the multilayer and monolayer models is stronger when using the $\mu(I)$-rheology. For instance, the multilayer approach changes the full deposit profiles for the $\mu(I)$-rheology, while it only changes the front position for μ_s. The multilayer approach makes it possible to obtain a deposit shape which is very close to the experiments with the $\mu(I)$-rheology. More generally, the shape of the deposit is closer to the observations with $\mu(I)$-MSM than with μ_s-MSM.

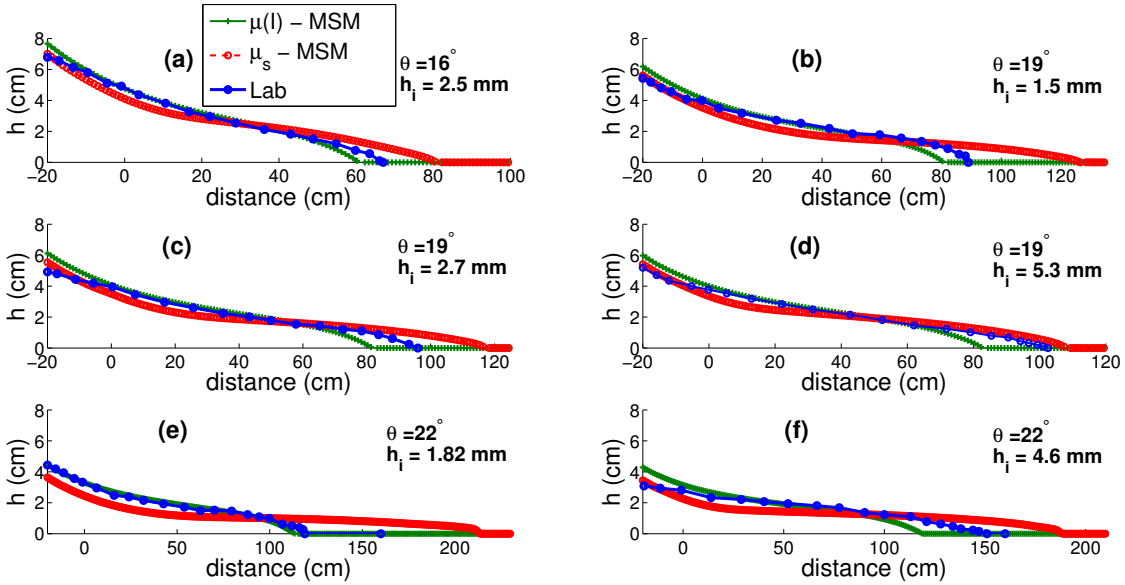

Figure 8: *Deposit obtained in the experiments (solid-circle blue line), with the μ_s-MSM (dotted-circle red line) and with the $\mu(I)$-MSM (solid-cross green line), for different slopes θ and erodible bed thicknesses h_i.*

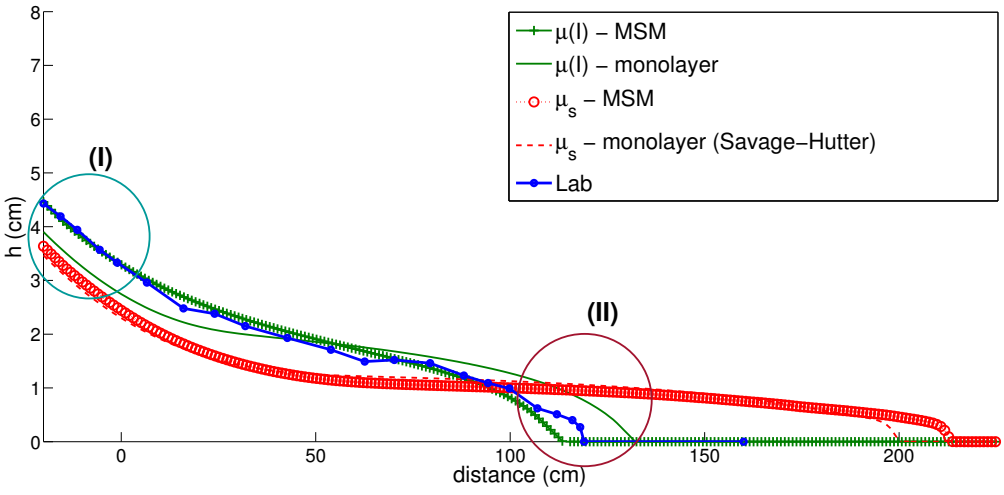

Figure 9: *Deposit obtained in the experiments (solid-circle blue line), with the μ_s-MSM (dotted-circle red line), the $\mu(I)$-MSM (solid-cross green line), the μ_s-monolayer model (dashed red line) and with the $\mu(I)$-monolayer model (solid green line) for a slope $\theta = 22°$ and an erodible bed thickness $h_i = 1.82$ mm. Circled sections indicates specific location for data shown in figure 10.*

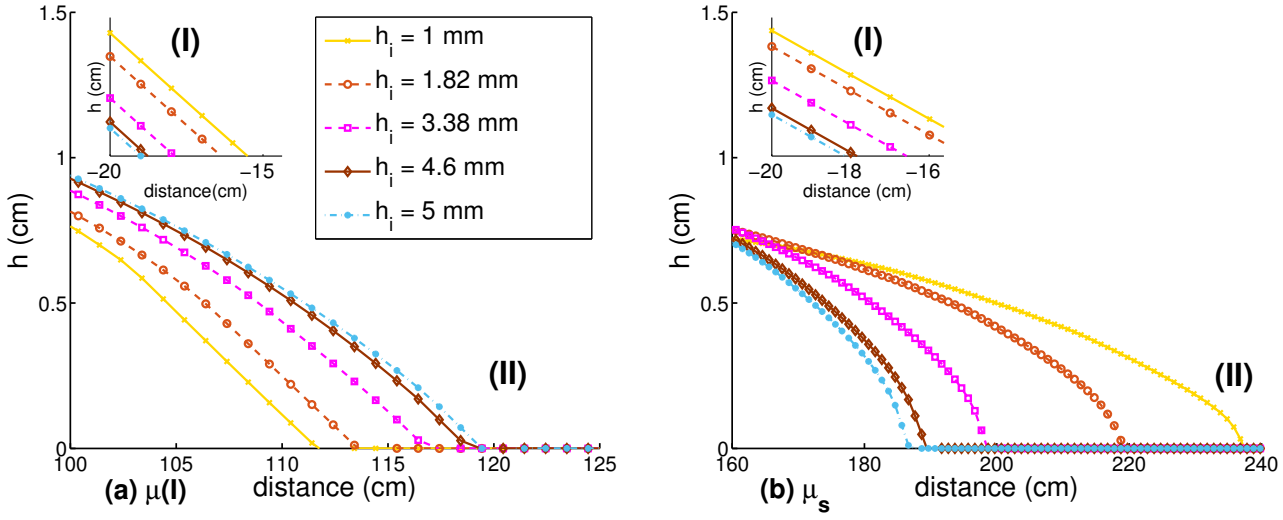

Figure 10: *Influence of the thickness of the erodible bed on the runout distance r_f and on the maximum final thickness h_f (inset graphs) with the $\mu(I)$-MSM (left hand side) and with the μ_s-MSM (right hand side), for a slope $\theta = 22°$, in zones marked with circle in figure 9.*

4.2.4 Effect of the erodible bed

Figure 10 shows two zooms, one near the maximum thickness of the deposit (zone of circle (I) in figure 9), and one near the front (zone of circle (II) in figure 9), for $\theta = 22°$ and different values of h_i. With the $\mu(I)$-MSM, the runout distance r_f increases as the thickness of the erodible bed h_i increases (figure 10a(II)) as observed in laboratory experiments. On the contrary, with the μ_s-MSM (figure 10b(II)), the runout distance r_f decreases with increasing h_i. Note that in both cases the maximum final thickness h_f decreases with increasing h_i as it occurs in the experiments (figure 10a(I),b(I)).

Figure 11 shows that the decrease in runout distance with increasing h_i for constant friction μ_s is observed for all slopes, e.g. $\theta = 0°$, $10°$, $16°$, $19°$, $22°$, and $23.7°$. For the constant friction coefficient case, the μ_s-MSM and μ_s-monolayer models follow the same trend. Note that this non-physical decrease in runout distance with increasing h_i has been demonstrated analytically in [20] for the monolayer model. Moreover, laboratory experiments show that when the thickness of the erodible bed increases, for slopes $\theta \geq \theta_c$, where $\theta_c \in [12°, 16°]$ is a critical slope, the runout distance r_f and the stopping time t_f both increase while the maximum final thickness h_f decreases. Note that there is no pattern concerning the runout when the thickness h_i is increased for slopes $\theta < \theta_c$ ($\theta = 0°$, $10°$) in the laboratory experiments.

Figure 12 shows that the increase of runout distance observed in the experiments for increasing h_i is qualitatively well reproduced with the $\mu(I)$-MSM. With the $\mu(I)$-MSM, the runout increase with h_i is actually larger for higher slopes, as observed experimentally: at $\theta = 16°$, the runout distance is almost unaffected by the thickness of the erodible bed while it increases by 26.9% at $\theta = 22°$ when the thickness of the erodible bed increase from 1.82 mm to 4.6 mm. Note that in the $\mu(I)$-MSM, the increase of the runout distance appears on slopes $\theta > 16°$, higher than θ_c in the experiments. Actually, it appears starting with the slope $\theta = 18°$. When using the $\mu(I)$-monolayer model, the runout distance is higher than for the $\mu(I)$-MSM whatever the slope and thickness of the erodible bed. Based on the values of the runout distance in these cases, it is hard to discriminate which of the monolayer or multilayer models is closer to the experiments. However, in the $\mu(I)$-monolayer model, the runout distance at $\theta = 16°$ and $19°$ decreases when h_i increases, contrary to the experimental data. For $\theta = 22°$ and $\theta = 23.7°$, the monolayer and multilayer $\mu(I)$

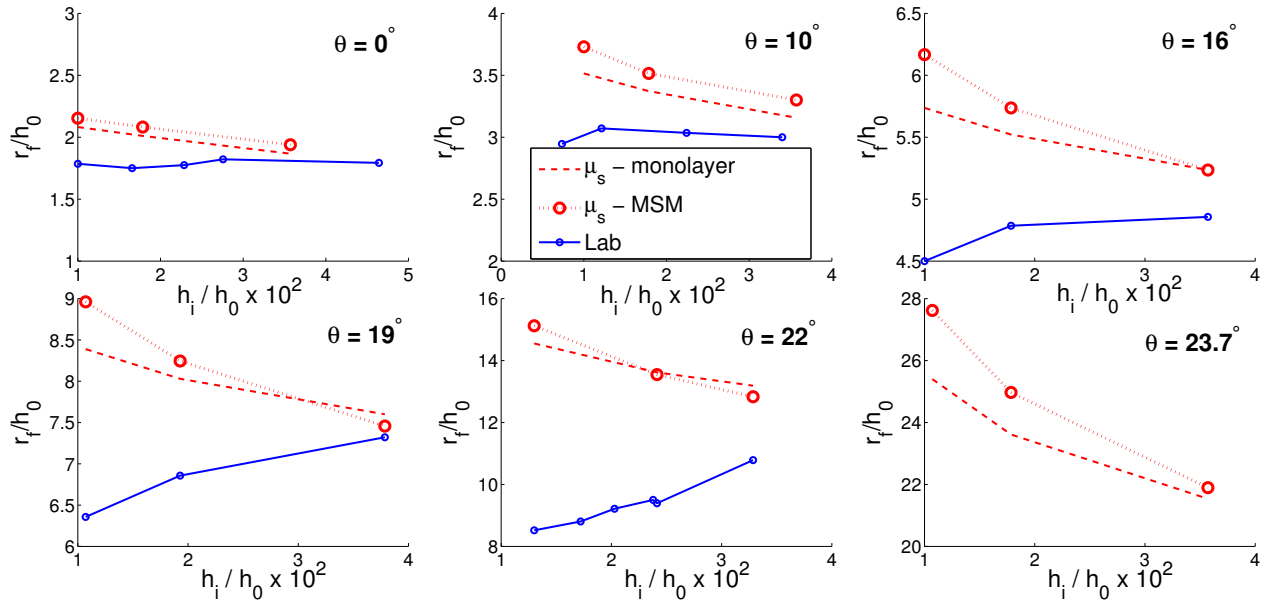

Figure 11: *Influence of the thickness h_i of the erodible bed on the final runout r_f for slopes $\theta = 0°, 10°, 16°, 19°, 22°, 23.7°$ observed in the experiments of [38] (solid-circle blue line) and obtained with different simulations using the μ_s-MSM, with 20 layers (dotted-circle red line) and the μ_s-monolayer model, i.e. the Savage-Hutter model (dashed red line). There is no laboratory data for $\theta = 23.7°$. Normalization is made using $h_0 = 14$ cm.*

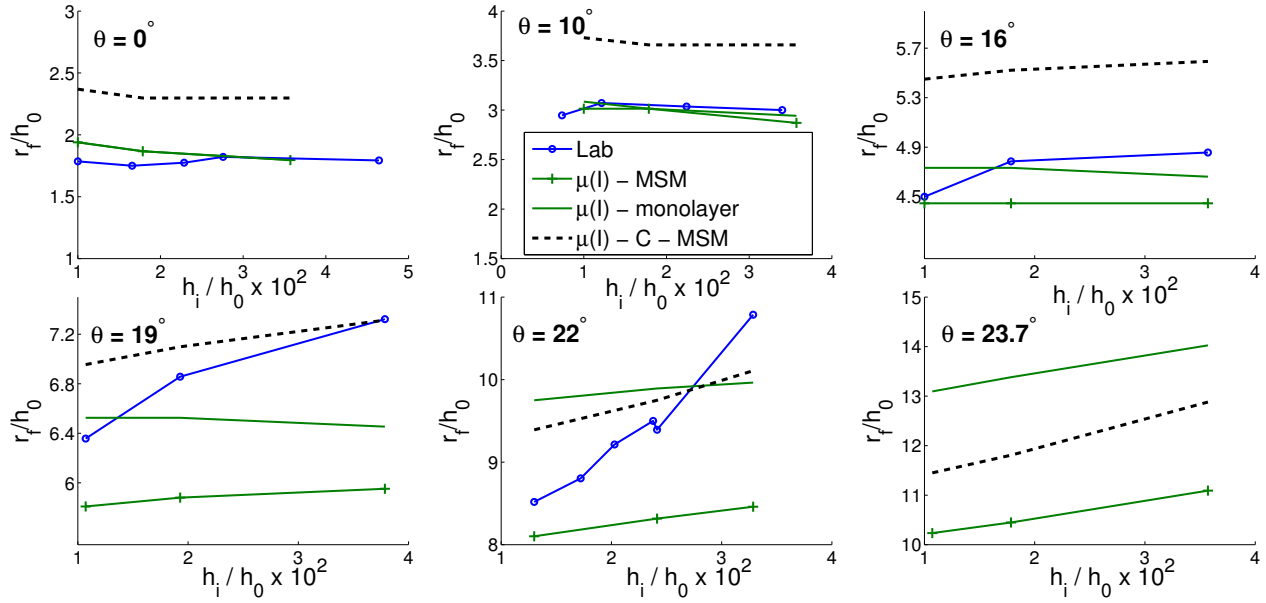

Figure 12: *Influence of the thickness h_i of the erodible bed on the final runout r_f for slopes $\theta = 16°, 19°, 22°, 23.7°$ observed in the experiments of [38] (solid-circle blue line) and obtained with different simulations using the $\mu(I)$-MSM, with 20 layers (solid-cross green line) and with the $\mu(I)$-monolayer model (solid green line) and with the $\mu(I)$-C-MSM (dashed black line). There is no laboratory data for $\theta = 23.7°$. Normalization is made using $h_0 = 14$ cm.*

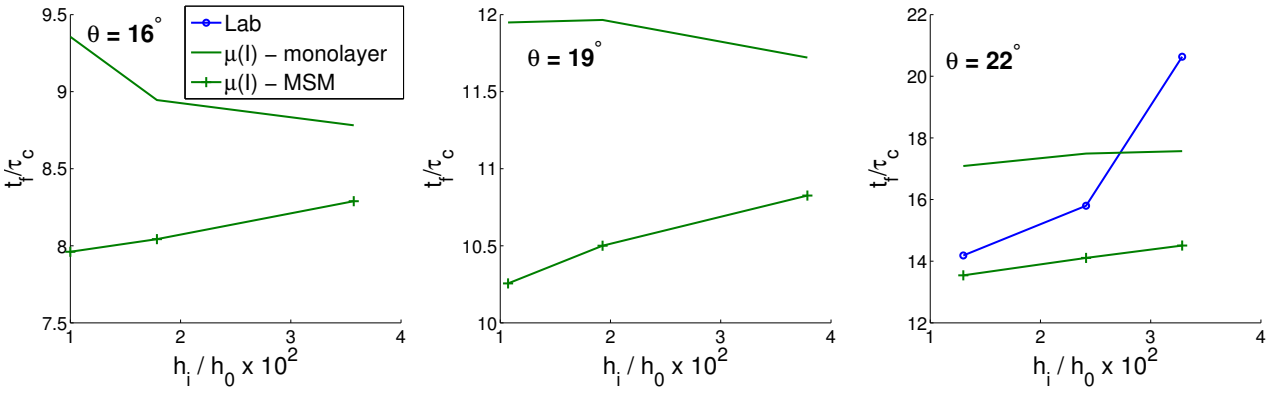

Figure 13: *Influence of the thickness h_i of the erodible bed on the final time t_f for slopes $\theta = 16°, 19°$ and $22°$ by using the $\mu(I)$-MSM with 20 layers (solid-cross green line), the $\mu(I)$-monolayer model (solid green line) and the values observed in the experiments of [38] for slope $\theta = 22°$ (solid-circle blue line). Normalization is made using $\tau_c = \sqrt{h_0/(g\cos\theta)}$ and $h_0 = 14$ cm.*

models reproduce qualitatively the increase in runout with h_i. Note that for $\theta = 0°, 10°$ ($\theta < \theta_c$), the $\mu(I)$ models predict a very slight decrease in the runout distance.

The $\mu(I)$-MSM is the model corresponding to the multilayer approach with the $\mu(I)$-rheology when $\|D(\boldsymbol{u})\|$ is approximated by the main term in (31), and $\mu(I)$-C-MSM when $\|D(\boldsymbol{u})\|$ is approximated by the correction (32). Figure 12 shows that the correction of $\|D(\boldsymbol{u})\|$ corresponding to $\mu(I)$-C-MSM improves the simulation of both the runout extent and the influence of the erodible bed. They both increase the runout when h_i increases, although the effect of erosion is still much smaller than in the experiments.

For example, for $\theta = 19^o$, when h_i varies from 1.5 mm to 5.3 mm, the experimental runout increases by 15.1%. On the contrary, for the monolayer model the runout decreases by 1.1%. For the $\mu(I)$-MSM the runout increases by 2.5%, and for the $\mu(I)$-C-MSM it increases by 6.8%. For $\theta = 22^o$, when h_i varies from 1.82 mm to 4.6 mm, the experimental runout increases by 26.9%. It increases by 2.2%, 4.4% and 8.6% for the monolayer model, the $\mu(I)$-MSM and the $\mu(I)$-C-MSM, respectively.

In figure 13, the final time (time at which the front stops) is plotted as a function of the thickness of the erodible bed for $\theta = 16^o$, $\theta = 19^o$ and $\theta = 22^o$. Moreover, for $\theta = 22^o$, we also plot the experimental data. Experimental data show that the final time increases when the thickness of the erodible bed increases. We can see that this is true for all the values of θ for the multilayer method. However, we observe that it is only true for the highest value, $\theta = 22^o$, in the case of the monolayer model, whereas the final time decreases when the erodible bed increases for $\theta = 16^o$ and $\theta = 19^o$.

4.2.5 Flow dynamics and velocity profiles

Figures 14 and 15 show the time evolution of the granular column thickness for a slope $\theta = 22°$ and an erodible bed of thickness $h_i = 1.82$ mm for μ_s and $\mu(I)$, respectively, for both the monolayer and multilayer models. As observed for the deposit, the difference between the thickness profiles simulated with the multilayer and the monolayer model is stronger for $\mu(I)$ than for μ_s. The $\mu(I)$-MSM makes it possible to increase the maximum thickness of the flow and decrease the thickness of the front. This is an important result as the shape of the front may be an indicator of the flow

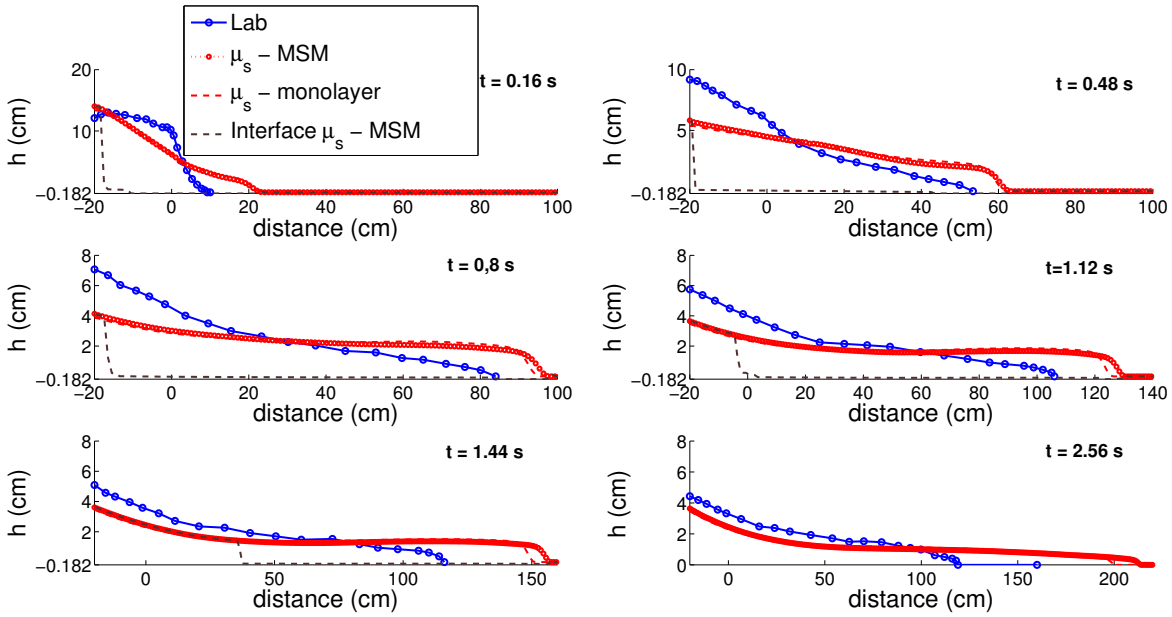

Figure 14: *Thickness of the granular mass at different times in the experiments (solid-circle blue line), with the μ_s-MSM with 20 layers (dotted-circle red line), with the μ_s-monolayer model (Savage-Hutter model, dashed red line) and the flow/non-flow interface (dashed-brown line), for the slope $\theta = 22^\circ$ and erodible bed thickness $h_i = 1.82$ mm.*

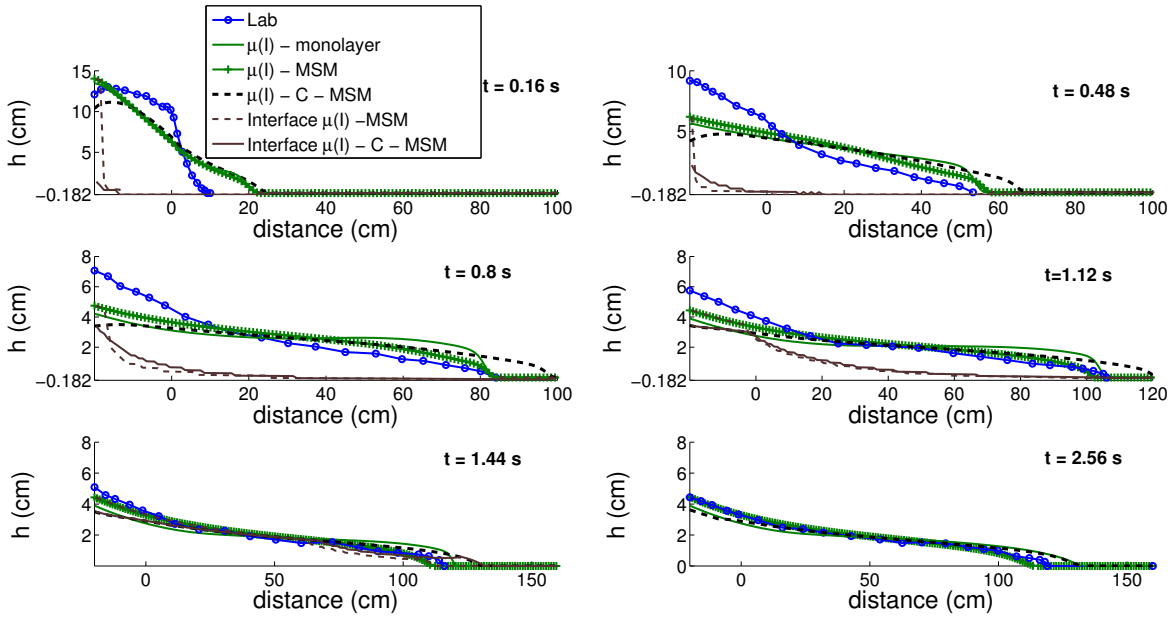

Figure 15: *Thickness of the granular mass at different times in the experiments (solid-circle blue line), with the $\mu(I)$-MSM using 20 layers (solid-cross green line), with the $\mu(I)$-monolayer model (solid green line), with the $\mu(I)$-C-MSM (dashed black line), and the flow/non-flow interface with both multilayer models (dashed-brown/solid-brown lines) for the slope $\theta = 22^\circ$ and erodible bed thickness $h_i = 1.82$ mm.*

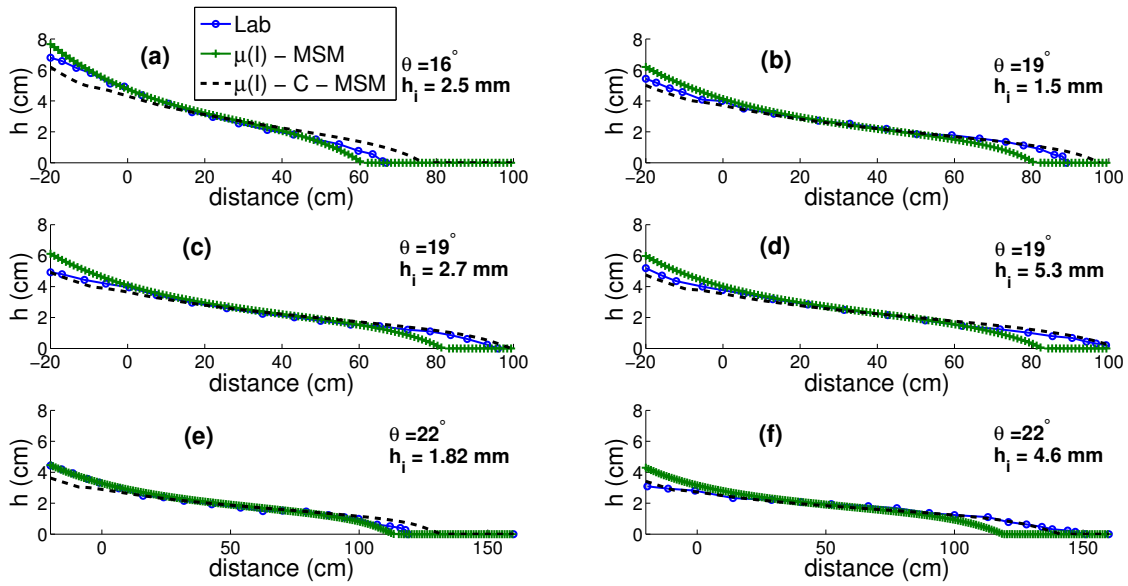

Figure 16: *Simulated deposits at different slopes θ and erodible bed thicknesses h_i with the $\mu(I)$-C-MSM (dashed black line) and the $\mu(I)$-MSM (solid-cross green line). The deposits observed in the experiments is represented by solid-circle blue lines.*

rheology ([43, 30]).

When a constant coefficient μ_s is used, very similar profiles are obtained with the μ_s-MSM and μ_s-monolayer model (Savage-Hutter model). As a result, the multilayer approach does not significantly improve the results when a constant friction coefficient is used. Note that during the initial instants, the simulated mass spreads faster than in the experiments. This is partly due to the role of initial gate removal that is not taken into account here. However, this effect does not explain the strong difference between the simulation and experiments (see [28] for more details). The hydrostatic assumption may also be responsible for this overestimation of the spreading velocity (see e.g. [39]). In these figures we also show the flow/no-flow interfaces computed with the multilayer models μ_s - MSM, $\mu(I)$ - MSM and $\mu(I)$ - C - MSM, by considering a threshold velocity of 0.001 m/s to compute these interfaces. We see in figure 14 that the flow/no-flow interface has a step-like shape for μ_s - MSM while it has a smoother shape for $\mu(I)$ - MSM (see figure 15) in better qualitative agreement with laboratory experiments and numerical modelling solving the full Navier-Stokes equations (e. g. figures 9 and 18 of [28]). The flow/no-flow interface in the uppermost part even seems to be improved when using $\mu(I)$ - C - MSM. For $\mu(I)$ - MSM and $\mu(I)$ - C - MSM, the lower layers stop before the upper layers as observed experimentally. Note that in figures 14 and 15 we do not see the flow/no-flow interface at the final time because the material has already stopped. As was shown in Subsection 4.1, the wall friction effect is crucial to determine the position of the flow/no-flow interface. Because in this test we do not consider the exact definition of the wall friction term, as in [28], the flow/no-flow interface should not be very well captured.

Figure 16 shows that the second-order correction in $\mu(I)$-C-MSM leads to simulated deposits that are generally closer to the experimental observations than those calculated with $\mu(I)$-MSM. In particular, the deposits at $\theta = 19°$ and $\theta = 22°$ with $h_i = 4.6$ mm are very well reproduced (figure 16b,c,d,f). However, in some cases, $\mu(I)$-MSM gives better results than $\mu(I)$-C-MSM, for example for $\theta = 22°$ with $h_i = 1.82$ mm. This is true for the overall dynamics as illustrated in figure 15 that shows the time change of the granular column thickness. We can see that with $\mu(I)$-

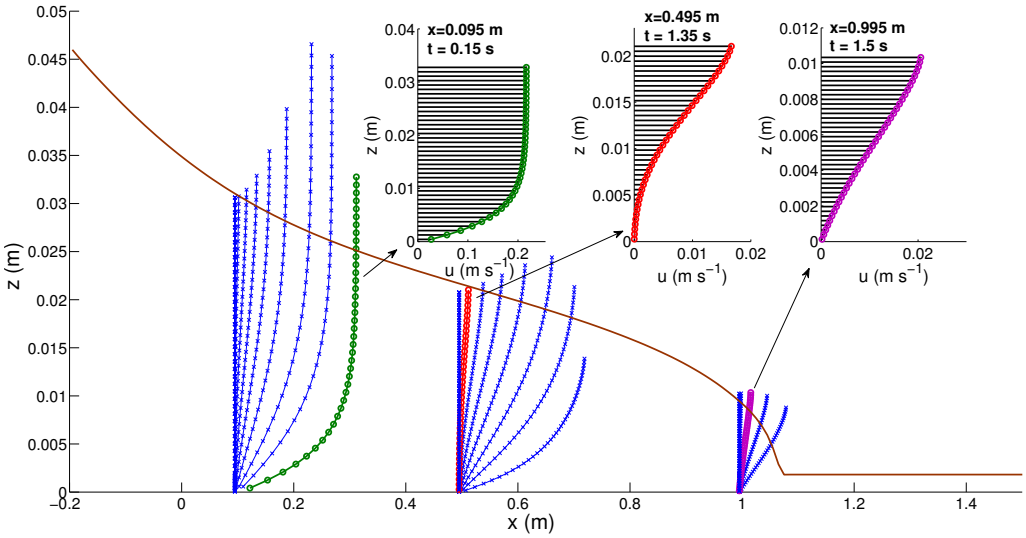

Figure 17: *Normal profiles of the downslope velocity obtained with the $\mu(I)$-MSM (40 layers) for $\theta = 22°$ and $h_i = 1.82$ mm during granular collapse at different positions ($x = 0.095$, 0.495, 0.995 m). For these positions, we represent the velocity profiles for different times, taken every 0.15 s (blue lines). The first selected profile (green) shows a profile at the beginning of the flow and the second (red) and third (magenta) profiles were measured during the stopping stage. The final deposit is represented by the solid brown line.*

C-MSM, the avalanche is faster and the runout is overestimated and very similar to the runout obtained with the $\mu(I)$ monolayer model. As other second-order terms than those included in the $\mu(I)$-C-MSM model are neglected, it is not easy to draw a firm conclusion on the improvement of results when using second-order terms.

The multilayer approach makes it possible to obtain a normal profile of the downslope velocity. Figures 17 and 18 show the normal profiles of the downslope velocity obtained at different times until the mass stops, for two different configurations of slopes and erodible beds. In order to obtain a more accurate profile, 40 layers are used in the $\mu(I)$-MSM. The different kind of profiles observed in figures 17 and 18 are in good qualitative agreement with typical velocity profiles of granular flows [24] (see also [35] and [36]), from Bagnold-like to S-shaped profiles. This shows the ability of the model to recover velocity profiles in a wide range of regimes.

Finally, let us compare the averaged velocity obtained with the $\mu(I)$-monolayer model to the average of the velocities over all the layers in the $\mu(I)$-MSM. In figure 17, for the green profile (respectively red and magenta profiles), the velocity in the monolayer model is 1.01 m/s (respectively 0.02 and 0.14 m/s) and it is 0.95 m/s in the multilayer model (respectively 0.03 and 0.05 m/s). Note that we obtain similar values for the first and second profiles. For the third profile, the averaged velocities strongly differ. Actually, at this position and time, the velocity profile corresponds to the stopping phase for the multilayer model but not for the monolayer model. As a result, the velocity obtained in the multilayer model is lower than that obtained in the monolayer model. Figure 19 shows the normal profile of normal velocity for the same configuration as figure 17. Note that the normal velocities are always negative and that their absolute values are greater in the upper layers.

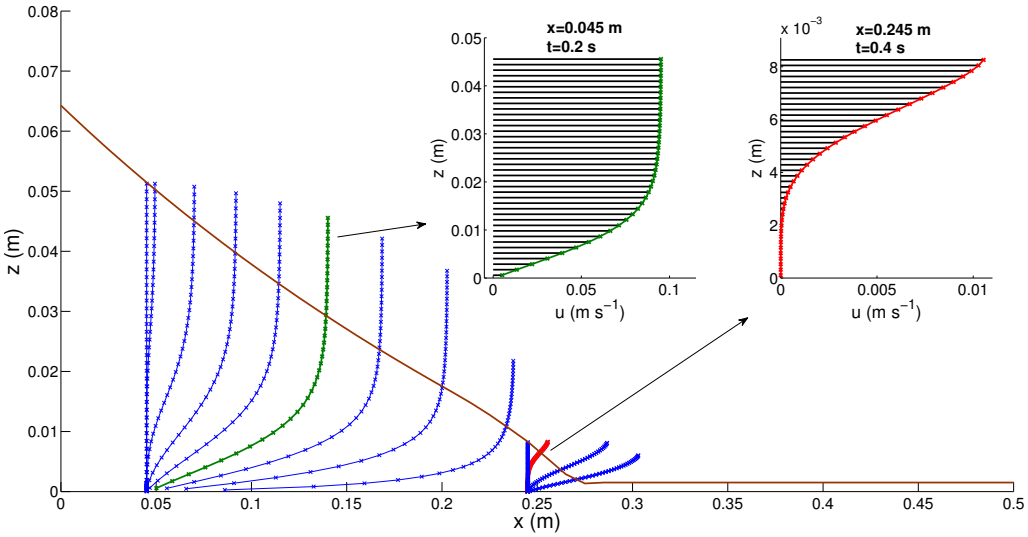

Figure 18: *Normal profiles of the downslope velocity obtained with the $\mu(I)$-MSM (40 layers) for $\theta = 0°$ and $h_i = 1.5$ mm during granular collapse at different positions ($x = 0.045, 0.245$ m) and times taken every 0.05 s.*

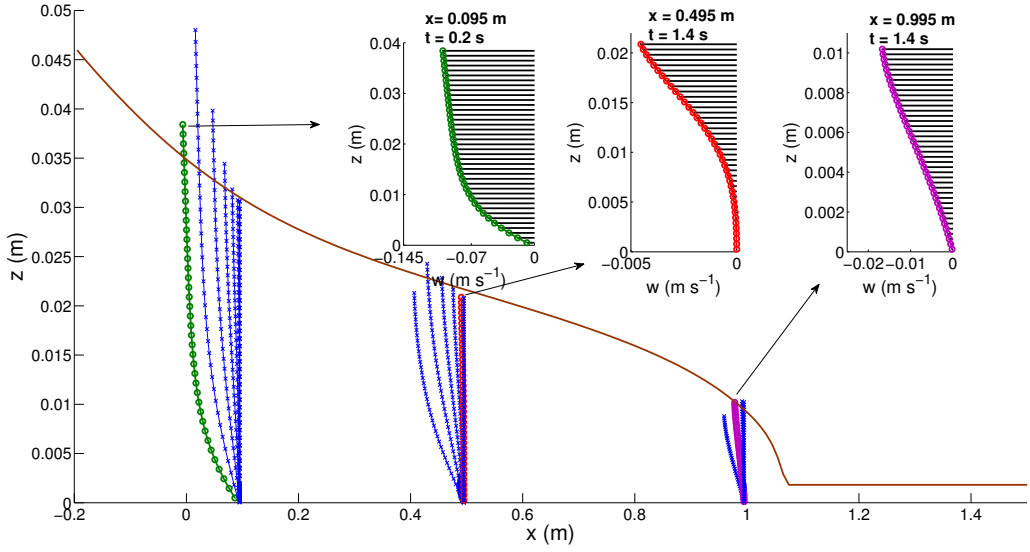

Figure 19: *Normal profiles of the normal velocity obtained with the $\mu(I)$-MSM (40 layers) for $\theta = 22°$ and $h_i = 1.82$ mm during granular collapse at different positions ($x = 0.095$, 0.495, 0.995 m) and times taken every 0.2 s.*

5 Conclusions

In this work, we have proposed a Multilayer Shallow Model for dry granular flows that considers a $\mu(I)$-rheology. The multilayer approach has been applied as in [23], thus leading to a solution of the resulting model that is a particular weak solution of the full Navier-Stokes equations with the $\mu(I)$-rheology. A regularization method has been used to avoid the singularity occurring when $\|D(\boldsymbol{u})\|$ vanishes. Our multilayer model satisfies a dissipative energy inequality, which is a requirement for a geophysical model to achieve a solution with physical meaning.

The numerical solutions of this model have been compared to the steady uniform Bagnold flow, whose analytical solution is known ([24, 49, 34]). The model has also been compared with analytical solution and laboratory experiments of granular surface flows in narrow channel, where the lateral walls have an important role in the velocity profile ([31, 33]). The MSM gives accurate approximations of these tests.

By comparing the numerical results obtained with this new model to laboratory experiments, we have shown that the model qualitatively and sometimes quantitatively reproduces the granular column collapses over inclined erodible beds performed in [38]. The increase of the runout distance with increasing thickness of the erodible bed is only reproduced when using the MSM with the $\mu(I)$-rheology ($\mu(I)$-MSM), although this increase is significantly underestimated. To our knowledge, this is the first time that a model has been able to reproduce this effect. The increase in runout distance appears for slopes $\theta \geq 18^\circ$ whereas it is observed for slopes $\theta \geq 16^\circ$ in the laboratory experiments. On the other hand, when using the $\mu(I)$-monolayer model, the increase of runout distance with the thickness of the erodible bed only occurs for slopes $\theta \geq 21^\circ$. Moreover, in the monolayer model for $\theta = 19^\circ$, the runout distance decreases as the thickness of the erodible bed increases, contrary to observations. As a result, when using the $\mu(I)$-rheology, the multilayer model significantly improves the simulated deposits at different slopes over different thicknesses of the erodible bed compared to the monolayer model. In particular it changes the shape of the front. This is an important result as the shape of the front may be an indicator of the flow rheology ([43, 30]).

When considering a constant friction coefficient, the multilayer approach only slightly changes the results compared to the monolayer model. Even with the multilayer model, the use of a constant friction coefficient does not make it possible to reproduce the increase in runout distance with increasing thickness of the erodible bed. In fact, the opposite effect is observed. This confirms the analytical results of [20] obtained for the monolayer Savage-Hutter equations. Furthermore the constant friction model strongly overestimates the front velocity and the runout distances. As a result, simulation of the effect of a thin erodible bed on the granular front dynamics in granular collapses and on their deposits seems to be a good test to discriminate between the different rheologies.

An important result is that this multilayer approach allows us to obtain the normal profiles of the downslope and normal velocities. These profiles qualitatively agree with the typical granular flow profiles during the developed flow and during the stopping phase [24]. In particular, the model makes it possible to reproduce the change from Bagnold-like to S-shaped velocity profiles, characteristic of flows over a rigid substrate and over a layer of static grains, respectively. As a result, this model should be applicable to a larger range of flow regimes than the depth-averaged models proposed by Capart *et al.* [14] and Edwards & Gray [19] for which velocity profiles are prescribed.

One of the differences between the multilayer and monolayer approaches is the accuracy of the approximation of the strain rate and consequently of the inertial number and the $\mu(I)$ friction coefficient. We have seen that the $\mu(I)$-C-MSM model, which introduces a second-order correction to improve the approximation of the strain rate, generally improves the results. The increase in runout distance when the thickness of the erodible bed is increased is larger and therefore closer to the laboratory experiments. In addition, the critical slope above which the runout increases

with the thickness of the erodible bed is $\theta \geq 16°$, which is closer to the value observed in the experiments than the critical slope predicted by the model without the second-order correction. This suggests that the extension of this shallow model up to the second order could be an important contribution.

Acknowledgements

This research has been partially supported by the Spanish Government and FEDER through the research project MTM2012-38383-C02-02, by the Andalusian Government through the project P11-RNM7069, by the ANR contract ANR-11-BS01-0016 LANDQUAKES, the USPC PEGES project and the ERC contract ERC-CG-2013-PE10-617472 SLIDEQUAKES.

A Derivation of the multilayer model

This appendix is dedicated to clarifying the complete derivation of the final model shown in subsection 3.3.

Let us consider the weak formulation of (16) in $\Omega_\alpha(t)$ for $\alpha = 1, ..., N$. We assume that the velocity $\boldsymbol{u}$, the pressure p and the density ρ are smooth in each $\Omega_\alpha(t)$ but may be discontinuous across the interfaces $\Gamma_{\alpha+1/2}$ for $\alpha = 1, ..., N-1$.
Assuming $\boldsymbol{u}_\alpha \in L^2(0,T;H^1(\Omega_\alpha(t))^2)$, $\partial_t \boldsymbol{u}_\alpha \in L^2(0,T;L^2(\Omega_\alpha(t))^2)$ and $p_\alpha \in L^2(0,T;L^2(\Omega_\alpha(t)))$, then a weak solution in $\Omega_\alpha(t)$ should satisfy

$$\left\{\begin{array}{rl} 0 = & \displaystyle\int_{\Omega_\alpha(t)} (\nabla\cdot\boldsymbol{u}_\alpha)\,\varphi\,d\Omega, \\ -\dfrac{1}{\varepsilon}\displaystyle\int_{\Omega_\alpha(t)} \rho\boldsymbol{f}\cdot\boldsymbol{v}\,d\Omega = & \displaystyle\int_{\Omega_\alpha(t)} \rho\partial_t\boldsymbol{u}_\alpha\cdot\boldsymbol{v}\,d\Omega + \int_{\Omega_\alpha(t)} \rho\Big(\boldsymbol{u}_\alpha\cdot\nabla\boldsymbol{u}_\alpha\Big)\cdot\boldsymbol{v}\,d\Omega + \\ & \displaystyle +\frac{1}{\varepsilon}\int_{\Omega_\alpha(t)} (\nabla\cdot(\mathcal{E}p_\alpha))\cdot\boldsymbol{v}\;d\Omega - \frac{1}{\varepsilon}\int_{\Omega_\alpha(t)} (\nabla\cdot(\boldsymbol{\tau}_{\varepsilon,\alpha}\,))\cdot\boldsymbol{v}\;d\Omega, \end{array}\right. \tag{33}$$

for all $\varphi \in L^2(\Omega_\alpha(t))$ and for all $\boldsymbol{v} \in H^1(\Omega_\alpha(t))^2$.

We consider unknowns, velocities and pressures, that satisfy (17) and the system (33) for test functions such that

$$\partial_z\varphi = 0$$

and

$$\boldsymbol{v}\,(t,x,z) = \Big(v\,(t,x),\ (z-b)\,V(t,x)\Big)', \qquad \boldsymbol{v}_{|_{\partial I_F(t)}} = 0, \tag{34}$$

where $v\,(t,x)$ and $V(t,x)$ are smooth functions that do not depend on z.

We will now develop (33) in order to obtain the mass and momentum conservation equations that satisfy the weak solution for this family of test functions for each layer.

A.1 Mass conservation

Similarly to the development in [23], we obtain the mass conservation law for each layer

$$\partial_t h_\alpha + \partial_x(h_\alpha u_\alpha) = G_{\alpha+\frac{1}{2}} - G_{\alpha-\frac{1}{2}}, \quad \alpha = 1, ..., N \tag{35}$$

where $G_{N+1/2}$ and $G_{1/2}$ stand for the mass exchange with the free surface and the bottom respectively and both should be given data.

A.2 Momentum conservation

Let $\boldsymbol{v} \in H^1(\Omega_\alpha)^2$ be a test function satisfying (34). We develop the momentum equation in (33) by integrating with respect to the variable z and by identifying the horizontal and vertical components of the vector test function $\boldsymbol{v}$. In addition, taking into account the hydrostatic pressure framework, we can leave out the equation corresponding to the vertical component. This is equivalent to considering the vector test function where the vertical component vanishes, i.e. $\boldsymbol{v} = (v\,(t,x), 0)$. Therefore, the horizontal momentum equation reads, for a weak solution $\boldsymbol{u}$ and for all $\alpha = 1, ..., N$:

$$\begin{aligned}
&-\frac{1}{\varepsilon}\int_{\Omega_\alpha(t)} \rho \boldsymbol{f} \cdot (v\,, 0)\, d\Omega = \int_{\Omega_\alpha(t)} \rho \partial_t(u_\alpha, \varepsilon w_\alpha) \cdot (v\,, 0)\, d\Omega + \\
&+ \int_{\Omega_\alpha(t)} \rho\Big((u_\alpha, \varepsilon w_\alpha) \cdot \nabla(u_\alpha, w_\alpha)\Big) \cdot (v\,, 0)\, d\Omega - \\
&-\frac{1}{\varepsilon}\int_{\Omega_\alpha(t)} (p_\alpha \mathcal{E}) : \nabla(v\,, 0)\, d\Omega + \frac{1}{\varepsilon}\int_{\Omega_\alpha(t)} \boldsymbol{\tau}_{\varepsilon,\alpha} : \nabla(v\,, 0)\, d\Omega + \\
&+\frac{1}{\varepsilon}\int_{\Gamma_{\alpha+\frac{1}{2}}(t)} \Big(\Big(-p_{\alpha+\frac{1}{2}}\mathcal{E} + \boldsymbol{\tau}^-_{\varepsilon,\alpha+\frac{1}{2}}\Big)\boldsymbol{n}_{\alpha+\frac{1}{2}}\Big) \cdot (v\,, 0)\, d\Gamma - \\
&-\frac{1}{\varepsilon}\int_{\Gamma_{\alpha-\frac{1}{2}}(t)} \Big(\Big(-p_{\alpha-\frac{1}{2}}\mathcal{E} + \boldsymbol{\tau}^+_{\varepsilon,\alpha-\frac{1}{2}}\Big)\boldsymbol{n}_{\alpha-\frac{1}{2}}\Big) \cdot (v\,, 0)\, d\Gamma.
\end{aligned} \tag{36}$$

We develop each term of this equation, taking into account that

$$\partial_z u_\alpha = \partial_z v\ = \boldsymbol{v}_{|_{\partial I_F(t)}} = 0.$$

The only terms that differ from those in [23] are those affected by the stress tensor. So we specify the development just for them. The rest of the terms in (36) follow the same pattern as in [23].

We prove that the term corresponding with the horizontal diffusion is a second-order term:

$$\frac{1}{\varepsilon}\int_{\Omega_\alpha(t)} \tau_{\varepsilon,xx,\alpha}\, \partial_x v\ \ d\Omega = \frac{1}{\varepsilon}\int_{I_F(t)} \left(\int_{z_{\alpha-1/2}}^{z_{\alpha+1/2}} \tau_{\varepsilon,xx,\alpha}\, \partial_x v\ \ dz\right) dx =$$

$$= \frac{1}{\varepsilon}\int_{I_F(t)} \left(\int_{z_{\alpha-1/2}}^{z_{\alpha+1/2}} \tau_{\varepsilon,xx,\alpha} dz \right) \partial_x v \, dx = -\frac{1}{\varepsilon}\int_{I_F(t)} \partial_x \left(\int_{z_{\alpha-1/2}}^{z_{\alpha+1/2}} \tau_{\varepsilon,xx,\alpha} \, dz \right) v \, dx +$$

$$+\frac{1}{\varepsilon}\int_{\partial I_F(t)} \left(\int_{z_{\alpha-1/2}}^{z_{\alpha+1/2}} \tau_{\varepsilon,xx,\alpha} \, dz \right) v \; \boldsymbol{n} \, d\Gamma = -\frac{1}{\varepsilon}\int_{I_F(t)} \partial_x \left(\int_{z_{\alpha-1/2}}^{z_{\alpha+1/2}} \tau_{\varepsilon,xx,\alpha} \, dz \right) v \, dx.$$

Because $\partial_z u_\alpha = 0$, we obtain that $\|D_\varepsilon(\boldsymbol{u}_\alpha)\|$ is independent of z up to order ε, since

$$D_\varepsilon(\boldsymbol{u}_\alpha) = \begin{pmatrix} \varepsilon^2 \partial_x u_\alpha & 0 \\ 0 & \partial_z w \end{pmatrix}.$$

Then, we get

$$\frac{1}{\varepsilon}\int_{z_{\alpha-\frac{1}{2}}}^{z_{\alpha+\frac{1}{2}}} \tau_{xx,\alpha} \, dz = \frac{1}{\varepsilon}\int_{z_{\alpha-\frac{1}{2}}}^{z_{\alpha+\frac{1}{2}}} \varepsilon^2 \eta \, \partial_x u_\alpha \, dz = O(\varepsilon).$$

Therefore, we can neglect this term since we are interested in the first-order model. Finally, the term that appears in the interfaces is written

$$\int_{\Gamma_{\alpha+\frac{1}{2}}(t)} \left(\left(-\mathcal{E} p_{\alpha+\frac{1}{2}} + \boldsymbol{\tau}^-_{\varepsilon,\alpha+\frac{1}{2}} \right) \boldsymbol{n}_{\alpha+\frac{1}{2}} \right) \cdot (v\,,0) \; d\Gamma \; =$$

$$= \int_{I_F(t)} \left(\left(-\mathcal{E} p_{\alpha+\frac{1}{2}} + \boldsymbol{\tau}^-_{\varepsilon,\alpha+\frac{1}{2}} \right) \boldsymbol{n}_{\alpha+\frac{1}{2}} \right) \cdot (v\,,0) \sqrt{1 + \left(\partial_x z_{\alpha+\frac{1}{2}} \right)^2} \, dx.$$

Note that $\dfrac{1}{\varepsilon}\mathcal{E} p_{\alpha+\frac{1}{2}} \boldsymbol{n}_{\alpha+\frac{1}{2}} \cdot (v\,,0) = p_{\alpha+\frac{1}{2}} \boldsymbol{n}_{\alpha+\frac{1}{2}} \cdot (v\,,0)$. Moreover,

$$\left(\boldsymbol{\tau}^-_{\varepsilon,\alpha+\frac{1}{2}} \boldsymbol{n}_{\alpha+\frac{1}{2}} \right) \cdot (v\,,0) \sqrt{1 + \left(\partial_x z_{\alpha+\frac{1}{2}} \right)^2} = \left(\tau^-_{\varepsilon,xx,\alpha+\frac{1}{2}} \partial_x z_{\alpha+\frac{1}{2}} - \tau^-_{\varepsilon,xz,\alpha+\frac{1}{2}} \right) v\,.$$

Introducing these calculations into (36) and taking into account that $\boldsymbol{f} = \left(\frac{\tan\theta}{Fr^2}, \; \frac{1}{Fr^2} \right)'$, we obtain

$$\int_{I_F(t)} \Bigg[\rho h_\alpha \partial_t u_\alpha + \rho h_\alpha u_\alpha \, \partial_x u_\alpha + \frac{\rho}{Fr^2} h_\alpha \partial_x \left(b + h \right) \; + \frac{1}{\varepsilon} \rho h_\alpha \frac{\tan\theta}{Fr^2} +$$

$$+ \frac{1}{\varepsilon} \left(\tau^-_{\varepsilon,xx,\alpha+\frac{1}{2}} \partial_x z_{\alpha+\frac{1}{2}} - \tau^-_{\varepsilon,xz,\alpha+\frac{1}{2}} \right) - \frac{1}{\varepsilon} \left(\tau^+_{\varepsilon,xx,\alpha-\frac{1}{2}} \partial_x z_{\alpha-\frac{1}{2}} - \tau^+_{\varepsilon,xz,\alpha-\frac{1}{2}} \right) \Bigg] \; v \, dx = 0\,.$$

And this yields, for each layer $\alpha = 1, \cdots, N$, the momentum equation

$$\rho h_\alpha \partial_t u_\alpha + \rho h_\alpha u_\alpha \, \partial_x u_\alpha + \frac{\rho}{Fr^2} h_\alpha \partial_x \left(b + h \right) + \rho \frac{1}{\varepsilon} h_\alpha \frac{\tan\theta}{Fr^2} +$$

$$+ \frac{1}{\varepsilon} \left(\tau^-_{\varepsilon,xx,\alpha+\frac{1}{2}} \partial_x z_{\alpha+\frac{1}{2}} - \tau^-_{\varepsilon,xz,\alpha+\frac{1}{2}} \right) - \frac{1}{\varepsilon} \left(\tau^+_{\varepsilon,xx,\alpha-\frac{1}{2}} \partial_x z_{\alpha-\frac{1}{2}} - \tau^+_{\varepsilon,xz,\alpha-\frac{1}{2}} \right) = 0.$$

Observe that

$$\tau^-_{\varepsilon,xx,\alpha+\frac{1}{2}}\partial_x z_{\alpha+\frac{1}{2}} - \tau^-_{\varepsilon,xz,\alpha+\frac{1}{2}} = \left[\boldsymbol{\tau}^-_{\varepsilon,\alpha+\frac{1}{2}}\boldsymbol{n}_{\alpha+\frac{1}{2}}\sqrt{1+\left(\partial_x z_{\alpha+\frac{1}{2}}\right)^2}\right]_H,$$

where $[\,\cdot\,]_H$ denotes the first component. Now by (21) we obtain

$$\left[\boldsymbol{\tau}^-_{\varepsilon,\alpha+\frac{1}{2}}\boldsymbol{n}_{\alpha+\frac{1}{2}}\sqrt{1+\left(\partial_x z_{\alpha+\frac{1}{2}}\right)^2}\right]_H = \left[\widetilde{\boldsymbol{\tau}}_{\varepsilon,\alpha+\frac{1}{2}}\boldsymbol{n}_{\alpha+\frac{1}{2}}\sqrt{1+\left(\partial_x z_{\alpha+\frac{1}{2}}\right)^2} - \frac{\varepsilon}{2}\rho G_{\alpha+\frac{1}{2}}\left[\boldsymbol{u}\right]_{|_{\Gamma_{\alpha+\frac{1}{2}}(t)}}\right]_H =$$

$$= \widetilde{\tau}_{\varepsilon,xx,\alpha+\frac{1}{2}}\partial_x z_{\alpha+\frac{1}{2}} - \widetilde{\tau}_{\varepsilon,xz,\alpha+\frac{1}{2}} - \frac{\varepsilon}{2}\rho G_{\alpha+\frac{1}{2}}\left(u_{\alpha+1}-u_\alpha\right),$$

and analogously

$$\left[\boldsymbol{\tau}^+_{\varepsilon,\alpha-\frac{1}{2}}\boldsymbol{n}_{\alpha-\frac{1}{2}}\sqrt{1+\left(\partial_x z_{\alpha-\frac{1}{2}}\right)^2}\right]_H = \widetilde{\tau}_{\varepsilon,xx,\alpha-\frac{1}{2}}\partial_x z_{\alpha-\frac{1}{2}} - \widetilde{\tau}_{\varepsilon,xz,\alpha-\frac{1}{2}} + \frac{\varepsilon}{2}\rho G_{\alpha-\frac{1}{2}}\left(u_\alpha-u_{\alpha-1}\right).$$

This allows us to rewrite the momentum equation as

$$\rho h_\alpha\partial_t u_\alpha + \rho h_\alpha u_\alpha\,\partial_x u_\alpha + \frac{\rho}{Fr^2}h_\alpha\partial_x\left(b+h\right) + \rho\frac{1}{\varepsilon}h_\alpha\frac{\tan\theta}{Fr^2} +$$

$$+\frac{1}{\varepsilon}\left(\widetilde{\tau}_{\varepsilon,xx,\alpha+\frac{1}{2}}\partial_x z_{\alpha+\frac{1}{2}} - \widetilde{\tau}_{\varepsilon,xz,\alpha+\frac{1}{2}}\right) - \frac{1}{\varepsilon}\left(\widetilde{\tau}_{\varepsilon,xx,\alpha-\frac{1}{2}}\partial_x z_{\alpha-\frac{1}{2}} - \widetilde{\tau}_{\varepsilon,xz,\alpha-\frac{1}{2}}\right) =$$

$$= \frac{1}{2}\rho G_{\alpha+\frac{1}{2}}\left(u_{\alpha+1}-u_\alpha\right) + \frac{1}{2}\rho G_{\alpha-\frac{1}{2}}\left(u_\alpha-u_{\alpha-1}\right).$$

Note that

$$\frac{1}{\varepsilon}\left(\widetilde{\tau}_{\varepsilon,xx,\alpha+\frac{1}{2}}\partial_x z_{\alpha+\frac{1}{2}} - \widetilde{\tau}_{\varepsilon,xz,\alpha+\frac{1}{2}}\right) = \frac{1}{\varepsilon}\left[\widetilde{\boldsymbol{\tau}}_{\varepsilon,\alpha+\frac{1}{2}}\boldsymbol{n}_{\alpha+\frac{1}{2}}\sqrt{1+\left(\partial_x z_{\alpha+\frac{1}{2}}\right)^2}\right]_H =$$

$$= \frac{1}{\varepsilon}\left[\eta\widetilde{D}_{\varepsilon,\alpha+\frac{1}{2}}\boldsymbol{n}_{\alpha+\frac{1}{2}}\right]_H\sqrt{1+\left(\partial_x z_{\alpha+\frac{1}{2}}\right)^2} = \varepsilon\eta_{\alpha+\frac{1}{2}}\partial_x\left(\frac{u^+_{\alpha+\frac{1}{2}}+u^-_{\alpha+\frac{1}{2}}}{2}\right)\partial_x z_{\alpha+\frac{1}{2}} -$$

$$-\varepsilon\eta_{\alpha+\frac{1}{2}}\left(\partial_x\left(\frac{w^+_{\alpha+\frac{1}{2}}+w^-_{\alpha+\frac{1}{2}}}{2}\right)\right)' - \frac{1}{\varepsilon}\eta_{\alpha+\frac{1}{2}}\mathcal{U}^H_{\mathcal{Z},\alpha+\frac{1}{2}}.$$

Now we define

$$K_{\alpha+\frac{1}{2}} = -\frac{1}{\varepsilon}\eta_{\alpha+\frac{1}{2}}\mathcal{U}^H_{\mathcal{Z},\alpha+\frac{1}{2}}, \tag{37}$$

where $\eta_{\alpha+\frac{1}{2}}$ is an approximation of η at $z = z_{\alpha+\frac{1}{2}}$ given by

$$\eta_{\alpha+\frac{1}{2}} = \frac{\mu(I_{\alpha+\frac{1}{2}})p_{\alpha+\frac{1}{2}}}{\max\left(\left|\mathcal{U}^H_{\mathcal{Z},\alpha+\frac{1}{2}}\right|, \frac{\mu(I_{\alpha+\frac{1}{2}})p_{\alpha+\frac{1}{2}}}{\eta_M}\right)},$$

with

$$p_{\alpha+\frac{1}{2}} = \frac{\rho}{Fr^2} \sum_{\beta=\alpha+1}^{N} h_\beta \,, \qquad I_{\alpha+\frac{1}{2}} = \frac{2\, d_s \left| \mathcal{U}^H_{\mathcal{Z}\,,\alpha+\frac{1}{2}} \right|}{\sqrt{p_{\alpha+\frac{1}{2}}/\rho_s}} \,.$$

These expressions of $\eta_{\alpha+\frac{1}{2}}$ and $I_{\alpha+\frac{1}{2}}$ are obtained from definitions (6) and (4), respectively, by considering the hydrostatic pressure approximation (18) with the definition of ρ, (5) and with the following first-order approximation of $\|D(\boldsymbol{u})\|$ at $z = z_{\alpha+\frac{1}{2}}$,

$$\|D(\boldsymbol{u})\|_{|z=z_{\alpha+\frac{1}{2}}} \approx \left| \mathcal{U}^H_{\mathcal{Z}\,,\alpha+\frac{1}{2}} \right| .$$

By combining the previous equation with (35) we get the momentum equation up to order ε,

$$\begin{aligned} &\rho \partial_t \left(h_\alpha u_\alpha\right) + \rho \partial_x (h_\alpha u_\alpha^2) + \frac{\rho}{Fr^2} h_\alpha \partial_x \left(b + h\right) + \rho \frac{1}{\varepsilon} h_\alpha \frac{tan\theta}{Fr^2} = \\ &= K_{\alpha-\frac{1}{2}} - K_{\alpha+\frac{1}{2}} + \frac{1}{2} \rho G_{\alpha+\frac{1}{2}} \left(u_{\alpha+1} + u_\alpha\right) - \frac{1}{2} \rho G_{\alpha-\frac{1}{2}} \left(u_\alpha + u_{\alpha-1}\right) , \end{aligned} \tag{38}$$

for $\alpha = 1, ..., N$.

Next, we must impose friction at the bottom ($\Gamma_{\alpha-\frac{1}{2}}$ with $\alpha = 1$). We can translate (14) into the notation of the multilayer approach, giving

$$w_{|\Gamma_{\frac{1}{2}}} = 0,$$

$$\frac{1}{\varepsilon} \eta_{\frac{1}{2}} \mathcal{U}^H_{\mathcal{Z}\,,\frac{1}{2}} = \frac{\mu\big(I_{\frac{1}{2}}\big)}{\varepsilon} p_{\frac{1}{2}} \frac{u^+_{\frac{1}{2}}}{\left| u^+_{\frac{1}{2}} \right|}.$$

Therefore to impose the friction condition, we should change definition (37) of $K_{\frac{1}{2}}$, taking into account that

$$u^+_{\frac{1}{2}} = u_1.$$

Then we obtain

$$K_{\frac{1}{2}} = -\frac{1}{\varepsilon} \eta_{\frac{1}{2}} \mathcal{U}^H_{\mathcal{Z}\,,\frac{1}{2}} = -\frac{\mu\big(I_{\frac{1}{2}}\big)}{\varepsilon} p_{\frac{1}{2}} \frac{u_1}{|u_1|}.$$

Finally, the final model (27) is obtained when we write (38) in dimensional variables.

References

[1] E. Audusse. A multilayer Saint-Venant model: derivation and numerical validation. *Discrete Contin. Dyn. Syst. Ser. B*, 5(2):189–214, 2005.

[2] E. Audusse, F. Bouchut, M. Bristeau, R. Klein, and B. Perthame. A fast and stable well-balanced scheme with hydrostatic reconstruction for shallow water flows. *SIAM Journal on Scientific Computing*, 25(6):2050–2065, 2004.

[3] E. Audusse, M. Bristeau, B. Perthame, and J. Sainte-Marie. A multilayer Saint-Venant system with mass exchanges for shallow water flows. derivation and numerical validation. *ESAIM: Mathematical Modelling and Numerical Analysis*, 45:169–200, 2011.

[4] E. Audusse, M-O. Bristeau, and A. Decoene. Numerical simulations of 3D free surface flows by a multilayer Saint-Venant model. *International journal for numerical methods in fluids*, 56(3):331–350, 2008.

[5] E. Audusse, M-O. Bristeau, M. Pelanti, and J. Sainte-Marie. Approximation of the hydrostatic Navier-Stokes system for density stratified flows by a multilayer model: kinetic interpretation and numerical solution. *Journal of Computational Physics*, 230(9):3453–3478, 2011.

[6] J. L. Baker, T. Barker, and J. M. N. T. Gray. A two-dimensional depth-averaged μ(I)-rheology for dense granular avalanches. *Journal of Fluid Mechanics*, 787:367–395, 1 2016.

[7] T. Barker, D. G. Schaeffer, P. Bohorquez, and J. M. N. T. Gray. Well-posed and ill-posed behaviour of the μ(I)-rheology for granular flow. *Journal of Fluid Mechanics*, 779:794–818, 9 2015.

[8] M. Bercovier and M. Engelman. A finite-element method for incompressible non-Newtonian flows. *Journal of Computational Physics*, 36(3):313 – 326, 1980.

[9] C. Berger, B. W. McArdell, and F. Schlunegger. Direct measurement of channel erosion by debris flows, illgraben, switzerland. *Journal of Geophysical Research: Earth Surface*, 116(F1), 2011. F01002.

[10] A. Bermúdez and C. Moreno. Duality methods for solving variational inequalities. *Computers & Mathematics with Applications*, 7(1):43–58, 1981.

[11] F. Bouchut. *Nonlinear Stability of Finite Volume Methods for Hyperbolic Conservation Laws: And Well-Balanced Schemes for Sources*. Springer Science & Business Media, 2004.

[12] F. Bouchut, E.D. Fernández-Nieto, A. Mangeney, and G. Narbona-Reina. A two-phase shallow debris flow model with energy balance. *ESAIM: M2AN*, 49(1):101–140, 2015.

[13] F. Bouchut, I. Ionescu, and A. Mangeney. An analytic approach for the evolution of the static-flowing interface in viscoplastic granular flows. *To appear in Comm. Math. Sci*, 2016.

[14] H. Capart, C.-Y. Hung, and C. P. Stark. Depth-integrated equations for entraining granular flows in narrow channels. *Journal of Fluid Mechanics*, 765, 2 2015.

[15] J. Chauchat and M. Médale. A three-dimensional numerical model for incompressible two-phase flow of a granular bed submitted to a laminar shearing flow. *Computer Methods in Applied Mechanics and Engineering*, 199(912):439 – 449, 2010.

[16] J. Chauchat and M. Médale. A three-dimensional numerical model for dense granular flows based on the μ(I)-rheology. *Journal of Computational Physics*, 256(0):696 – 712, 2014.

[17] S. J. Conway, A. Decaulne, M. R. Balme, J. B. Murray, and M. C. Towner. A new approach to estimating hazard posed by debris flows in the westfjords of iceland. *Geomorphology*, 114(4):556–572, 2010.

[18] R. Delannay, A. Valance, A. Mangeney, O. Roche, and P. Richard. Granular and particle-laden flows: from laboratory experiments to field observations. *Submitted to Journal of Physics D: Applied Physics*, 2015.

[19] A. N. Edwards and J.M.N.T. Gray. Erosion-deposition waves in shallow granular free-surface flows. *Journal of Fluid Mechanics*, 762:35–67, January 2015.

[20] G. Faccanoni and A. Mangeney. Exact solution for granular flows. *International Journal for Numerical and Analytical Methods in Geomechanics*, 37(10):1408–1433, 2013.

[21] M. Farin, A. Mangeney, and O. Roche. Fundamental changes of granular flow dynamics, deposition, and erosion processes at high slope angles: Insights from laboratory experiments. *Journal of Geophysical Research: Earth Surface*, 119(3):504–532, 2014.

[22] E.D. Fernández-Nieto, F. Bouchut, D. Bresch, M.J. Castro Díaz, and A. Mangeney. A new Savage-Hutter type model for submarine avalanches and generated tsunami. *Journal of Computational Physics*, 227(16):7720 – 7754, 2008.

[23] E.D. Fernández-Nieto, E.H. Koné, and T. Chacón Rebollo. A Multilayer Method for the Hydrostatic Navier-Stokes Equations: A Particular Weak Solution. *Journal of Scientific Computing*, 60(2):408–437, 2014.

[24] GDR MiDi. On dense granular flows. *The European Physical Journal E*, 14(4):341–365, 2004.

[25] R. Glowinski and P. Le Tallec. Augmented Lagrangian and operator-splitting methods in nonlinear mechanics. *SIAM Publication Co*, 1989.

[26] J. M. N. T. Gray and A. N. Edwards. A depth-averaged μ(I)-rheology for shallow granular free-surface flows. *Journal of Fluid Mechanics*, 755:503–534, 2014.

[27] J. M. N. T. Gray, Y.-C. Tai, and S. Noelle. Shock waves, dead zones and particle-free regions in rapid granular free-surface flows. *Journal of Fluid Mechanics*, 491:161–181, 9 2003.

[28] I.R. Ionescu, A. Mangeney, F. Bouchut, and R. Roche. Viscoplastic modeling of granular column collapse with pressure-dependent rheology. *Journal of Non-Newtonian Fluid Mechanics*, 219(0):1 – 18, 2015.

[29] R. M. Iverson, M. E. Reid, M. Logan, R. G. LaHusen, J. W. Godt, and J. P. Griswold. Positive feedback and momentum growth during debris-flow entrainment of wet bed sediment. *Nature Geoscience*, 4(2):116 – 121, 2011.

[30] D.E. Jessop, K. Kelfoun, P. Labazuy, A. Mangeney, O. Roche, J.-L. Tillier, M. Trouillet, and G. Thibault. LiDAR derived morphology of the 1993 Lascar pyroclastic flow deposits, and implication for flow dynamics and rheology. *Journal of Volcanology and Geothermal Research*, 245-246(0):81 – 97, 2012.

[31] P. Jop, Y. Forterre, and O. Pouliquen. Crucial role of sidewalls in granular surface flows: consequences for the rheology. *Journal of Fluid Mechanics*, 541:167–192, 10 2005.

[32] P. Jop, Y. Forterre, and O. Pouliquen. A constitutive law for dense granular flows. *Nature*, 441(7094):727–730, 2006.

[33] P. Jop, Y. Forterre, and O. Pouliquen. Initiation of granular surface flows in a narrow channel. *Physics of Fluids (1994-present)*, 19(8):088102, 2007.

[34] P.-Y. Lagrée, L. Staron, and S. Popinet. The granular column collapse as a continuum: validity of a two-dimensional Navier-Stokes with a μ(I)-rheology. *Journal of Fluid Mechanics*, 686:378–408, 2011.

[35] C. Lusso, F. Bouchut, A. Ern, and A. Mangeney. A simplified model for static/flowing dynamics in thin-layer flows of granular materials with yield. April 2015.

[36] C. Lusso, A. Ern, F. Bouchut, A. Mangeney, M. Farin, and O. Roche. Two-dimensional simulation by regularization of free surface viscoplastic flows with Drucker-Prager yield stress and application to granular collapse. March 2015.

[37] A. Mangeney, F. Bouchut, N. Thomas, J. P. Vilotte, and M. O. Bristeau. Numerical modeling of self-channeling granular flows and of their levee-channel deposits. *Journal of Geophysical Research: Earth Surface*, 112(F2):n/a–n/a, 2007. F02017.

[38] A. Mangeney, O. Roche, O. Hungr, N. Mangold, G. Faccanoni, and A. Lucas. Erosion and mobility in granular collapse over sloping beds. *Journal of Geophysical Research: Earth Surface (2003–2012)*, 115(F3), 2010.

[39] A. Mangeney-Castelnau, F. Bouchut, J. P. Vilotte, E. Lajeunesse, A. Aubertin, and M. Pirulli. On the use of Saint-Venant equations to simulate the spreading of a granular mass. *Journal of Geophysical Research: Solid Earth*, 110(B9), 2005.

[40] A. Mangeney-Castelnau, J.-P. Vilotte, M. O. Bristeau, B. Perthame, F. Bouchut, C. Simeoni, and S. Yerneni. Numerical modeling of avalanches based on Saint Venant equations using a kinetic scheme. *Journal of Geophysical Research: Solid Earth*, 108(B11):n/a–n/a, 2003. 2527.

[41] C. Parés. Numerical methods for nonconservative hyperbolic systems: a theoretical framework. *SIAM Journal on Numerical Analysis*, 44(1):300–321, 2006.

[42] M. Pirulli and A. Mangeney. Results of back-analysis of the propagation of rock avalanches as a function of the assumed rheology. *Rock Mechanics and Rock Engineering*, 41(1):59–84, 2008.

[43] O. Pouliquen. On the shape of granular fronts down rough inclined planes. *Physics of Fluids*, 11(7), 1999.

[44] O. Pouliquen. Scaling laws in granular flows down rough inclined planes. *Physics of Fluids (1994-present)*, 11(3):542–548, 1999.

[45] O. Pouliquen and Y. Forterre. Friction law for dense granular flows: application to the motion of a mass down a rough inclined plane. *Journal of Fluid Mechanics*, 453:133–151, 2002.

[46] J. Sainte-Marie. Vertically averaged models for the free surface non-hydrostatic Euler system: derivation and kinetic interpretation. *Mathematical Models and Methods in Applied Sciences*, 21(03):459–490, 2011.

[47] S. B. Savage and K. Hutter. The motion of a finite mass of granular material down a rough incline. *Journal of Fluid Mechanics*, 199:177–215, 2 1989.

[48] D. Schaeffer. Instability in the evolution equations describing incompressible granular flow. *Journal of Differential Equations*, 66(1):19 – 50, 1987.

[49] L. E. Silbert, D. Ertaş, G. S. Grest, T. C. Halsey, D. Levine, and S. J. Plimpton. Granular flow down an inclined plane: Bagnold scaling and rheology. *Phys. Rev. E*, 64:051302, Oct 2001.

[50] L. Staron, P.-Y. Lagrée, and S. Popinet. The granular silo as a continuum plastic flow: The hour-glass vs the clepsydra. *Physics of Fluids (1994-present)*, 24(10), 2012.

[51] L. Staron, P.-Y. Lagrée, and S. Popinet. Continuum simulation of the discharge of the granular silo: A validation test for the μ(I)-visco-plastic flow law. *The European physical journal. E, Soft matter*, 37(1), 2014.